Crystallization depth beneath an oceanic detachment fault (ODP Hole 923A, Mid-Atlantic Ridge)

AGU PUBLICATIONS

Geochemistry, Geophysics, Geosystems

RESEARCH ARTICLE
10.1002/2015GC006027

Crystallization depth beneath an oceanic detachment fault (ODP Hole 923A, Mid-Atlantic Ridge)

C. Johan Lissenberg[1], Matthew Rioux[2], Christopher J. MacLeod[1], Samuel A. Bowring[3], and Nobumichi Shimizu[4]

[1]School of Earth and Ocean Sciences, Cardiff University, Cardiff, UK, [2]Earth Research Institute, University of California, Santa Barbara, California, USA, [3]Department of Earth, Atmospheric, and Planetary Sciences, Massachusetts Institute of Technology, Cambridge, Massachusetts, USA, [4]Woods Hole Oceanographic Institution, Woods Hole, Massachusetts, USA

Key Points:
- Crystallization depths beneath a detachment-dominated ridge segment have been determined
- Best estimate of crystallization depth is 6.4 +1.7/−1.3 km
- Parental magma emplaced up to 1.5 km deeper at <8 km

Correspondence to:
C. J. Lissenberg,
lissenbergcj@cardiff.ac.uk

Citation:
Lissenberg, C. J., M. Rioux, C. J. MacLeod, S. A. Bowring, and N. Shimizu (2016), Crystallization depth beneath an oceanic detachment fault (ODP Hole 923A, Mid-Atlantic Ridge), *Geochem. Geophys. Geosyst.*, *17*, 162–180, doi:10.1002/2015GC006027.

Received 22 JUL 2015
Accepted 11 DEC 2015
Accepted article online 15 DEC 2015
Published online 21 JAN 2016

Abstract Oceanic detachment faults are increasingly recognized as playing an integral role in the seafloor spreading process at slow and ultraslow spreading mid-ocean ridges, with significant consequences for the architecture of the oceanic lithosphere. Although melt supply is considered to play a critical control on the formation and evolution of oceanic detachments, much less well understood is how melts and faults interact and influence each other. Few direct constraints on the locus and depth of melt emplacement in the vicinity of detachments are available. Gabbros drilled in ODP Hole 923A near the intersection of the Mid-Atlantic Ridge and the Kane transform fault (23°N; the MARK area) represent magmas emplaced into the footwall of such a detachment fault and unroofed by it. We here present U-Pb zircon dates for these gabbros and associated diorite veins which, when combined with a tectonic reconstruction of the area, allow us to calculate the depths at which the melts crystallized. Th-corrected single zircon U-Pb dates from three samples range from 1.138 ± 0.062 to 1.213 ± 0.021 Ma. We find a crystallization depth of 6.4 +1.7/−1.3 km, and estimate that the melts parental to the gabbros were initially emplaced up to 1.5 km deeper, at <8 km below the seafloor. The tectonic reconstruction implies that the detachment fault responsible for the exposure of the sampled sequence likely crossed the ridge axis at depth, suggesting that melt emplacement into the footwall of oceanic detachment faults is an important process. The deep emplacement depth we find associated with "detachment mode" spreading at ~1.2 Ma appears to be significantly greater than the depth of magma reservoirs during the current "magmatic mode" of spreading in the area, suggesting that the northern MARK segment preserves a recent switch between two temporally distinct modes of spreading with fundamentally different lithospheric architecture.

1. Introduction

Detachment faulting, whereby the plutonic basement of a spreading ridge is exhumed on the seafloor along long-lived, large-offset normal faults, plays a fundamental role during oceanic crustal accretion at slow and ultraslow spreading mid-ocean ridges [*Dick et al*., 1981; *Tucholke and Lin*, 1994; *Cann et al*., 1997; *Karson and Lawrence*, 1997a; *Tucholke et al*., 1998; *MacLeod et al*., 2002, 2009; *Escartín and Canales*, 2011]. Initially thought to be restricted to the vicinity of ridge-transform intersections [*Dick et al*., 1981; *Tucholke and Lin*, 1994], and associated with formation of oceanic core complexes [e.g., *Cann et al*., 1997], detachment faulting is now believed to be more widespread, potentially occurring along large sections of the Earth's slow and ultraslow spreading ridge system [*Okino et al*., 2004; *Cannat et al*., 2006; *Smith et al*., 2006; *Escartin et al*., 2008; *Sauter et al*., 2013; *Cann et al*., 2015]. Detachment faults may take up significant proportions, or even all, of plate separation, leading to asymmetric spreading [*Allerton et al*., 2000; *Searle et al*., 2003; *Baines et al*., 2008; *Grimes et al*., 2008]. In addition, detachment faults act to focus hydrothermal fluids [*McCaig et al*., 2007]. Finally, they generate invaluable tectonic windows into both the lower crustal magmatic plumbing system and the underlying upper mantle [*Dick et al*., 2000, 2008; *Blackman et al*., 2011]. As such, detachment faulting plays an integral role in the seafloor spreading process and strongly influences the mechanisms of crustal accretion at slow and ultraslow spreading ridges.

One of the critical factors controlling the formation and evolution of oceanic detachment faults is melt supply. Numerical models have shown that high-angle normal faults are able to develop into long-lived low-angle detachment faults when magmatic accretion accounts for approximately one third to half of the extension at

a spreading ridge, with the remainder being taken up by faulting [*Buck et al*., 2005; *Behn and Ito*, 2008; *Tucholke et al*., 2008]. In addition to the amount of melt supplied to the ridge, it is now recognized that the locus of this supply must also be a key factor in controlling detachment fault development [*MacLeod et al*., 2009; *Olive et al*., 2010]; however, there are currently few direct constraints on where melt is emplaced, and particularly the depth at which this occurs, beneath detachment-dominated ridge segments.

Existing constraints on the depths of melt emplacement beneath detachment-dominated ridge segments come primarily from microseismicity and studies of unroofed gabbroic sections. Microearthquake depths provide information on the depth of the brittle-ductile transition (i.e., crustal temperatures >600–800°C) [*Harper*, 1985], and, by extension, the thermal structure of the oceanic lithosphere. Microearthquakes for Mid-Atlantic Ridge segment ends (29°N) [*Wolfe et al*., 1995] and detachment faults (TAG) [*Kong et al*., 1992; *deMartin et al*., 2007] cluster between ~4 and 7 km depth, suggesting that the lithosphere is relatively cool, promoting melt emplacement in the deep crust or the mantle lithosphere, although thermal structures are likely to be transient and spatially and temporally variable at slow spreading ridges. *Grimes et al*. [2011] and *Schoolmeesters et al*. [2012] combined thermal histories (derived from U-Pb and (U-Th)/He dating of zircon) of gabbroic rocks with models for detachment fault geometry and plate spreading rate to estimate the depth of the 850°C isotherm along oceanic detachment faults along the Mid-Atlantic Ridge near the Fifteen Twenty and Atlantis fracture zones. They determined these depths to be ~7 km, and inferred that this represents a minimum emplacement depth of the gabbroic plutons.

In this contribution, we combine high-precision zircon geochronology with tectonic and spreading rate reconstructions from the MARK area (23°N, Mid-Atlantic Ridge) in an alternative and more direct method of determining the crystallization depth of gabbro and diorite veins exposed in the footwall of an oceanic detachment fault. Our calculations suggest that the crystallization depth of the plutonic rocks was 6.4 +1.7/−1.3 km, and we estimate that the initial emplacement of their parental melt occurred up to 1.5 km deeper.

2. The MARK Area

2.1. Geology of the MARK Area

The Mid-Atlantic Ridge south of the Kane transform (the MARK area, 23°N) is one of the best-studied ridge sections worldwide. The area has been subject to numerous bathymetric [*Pockalny et al*., 1988; *Gente et al*., 1995], submersible [*Karson and Dick*, 1983; *Gente et al*., 1991; *Mével et al*., 1991; *Auzende et al*., 1994], camera [*Karson and Dick*, 1983], and geophysical [*Detrick and Purdy*, 1980; *Purdy and Detrick*, 1986; *Kong et al*., 1988; *Schulz et al*., 1988; *Detrick et al*., 1990; *Ballu et al*., 1998; *Williams*, 2007] surveys, as well as three ODP drilling legs (Legs 106/109 [*Detrick et al*., 1988] and Leg 153 [*Cannat et al*., 1995]).

Immediately south of the transform, the ridge is comprised of two spreading segments, separated by a non-transform offset at 23°05–23°17′N [*Purdy and Detrick*, 1986; *Karson et al*., 1987; *Brown and Karson*, 1988; *Kong et al*., 1988; *Schulz et al*., 1988]. The ridge axis of the northern segment (Figure 1) is characterized by a prominent axial volcanic ridge (AVR) called Snake Pit [*Kong et al*., 1988; *Gente et al*., 1991]. The occurrence of active hydrothermal fields near its summit, as well as the presence of fresh and unsedimented basaltic lavas, indicate that the Snake Pit AVR is the locus of active volcanism [*Karson and Brown*, 1988; *Kong et al*., 1988; *Gente et al*., 1991]. This is consistent with the young U-series dates (~10,000 years) of its lavas [*Sturm et al*., 2000]. Seismic data indicate that the igneous crust beneath the Snake Pit AVR is ~5.5 km thick, with partial melt inferred to be present at depths of >2 km [*Canales et al*., 2000]. This is in strong contrast to the thin crust (<2.5 km) on the flanks of the axial valley wall inferred from seismic data [*Canales et al*., 2000]. These data suggest that the northern MARK segment switched from a magma-starved to a magmatically robust mode of crustal accretion around 400 ka, with the Snake Pit AVR accommodating present-day crustal accretion [*Canales et al*., 2000]. Toward the transform, the Snake Pit AVR narrows and deepens, bending around the eastern side of the deep (~6200 mbsl) nodal basin at the ridge-transform intersection [*Pockalny et al*., 1988]. The Snake Pit AVR is flanked by older, more sedimented lavas on the axial valley floor [*Karson et al*., 1987; *Gente et al*., 1991], along with a number of volcanic cones [*Kong et al*., 1988].

The ridge-transform intersection (RTI) is characterized by a strong morphological and tectonic asymmetry, similar to that described for many slow spreading RTIs [*Severinghaus and Macdonald*, 1988]. The outside corner is dominated by rough, but overall relatively flat terrain at ~3500 mbsl, and is comprised of elongate ridges of basaltic lavas crosscut by ridge-parallel high-angle normal faults. Seafloor morphology suggests

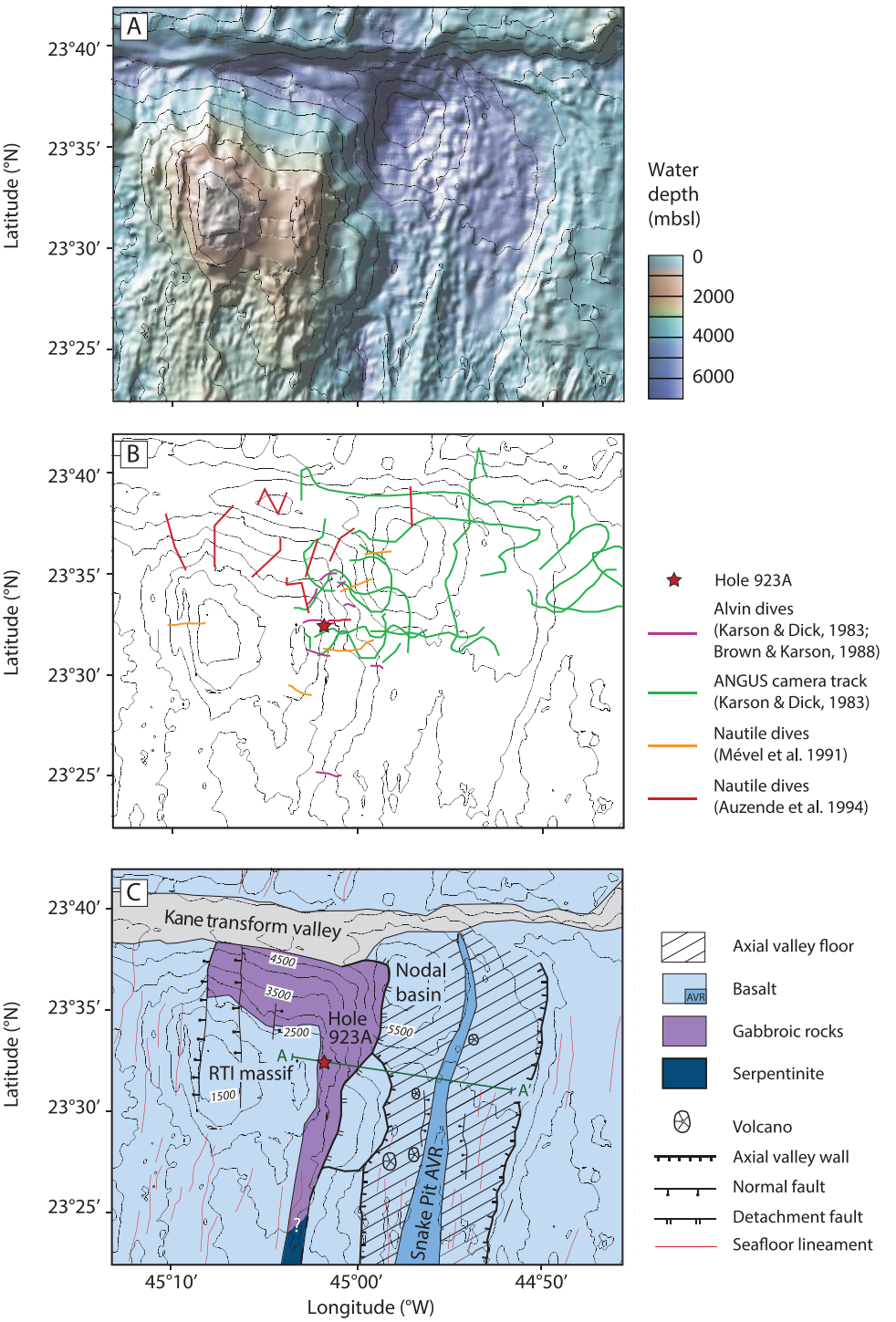

Figure 1. (a) Bathymetry of the eastern intersection of the Mid-Atlantic Ridge with the Kane transform fault, illustrating the seafloor morphology. Bathymetry map was generated using GeoMapApp (http://www.geomapapp.org) using the GMRT grid [*Ryan et al*., 2009]. Contour interval 500 m. (b) Slope map of the area shown in Figure 1a, illustrating the locations of on-bottom observations. (c) Interpretative geological map of the area shown in Figure 1a, showing the location of elements discussed in this paper. A-A′ marks the location of the profile of Figure 2. Geology based on published data [*Karson and Dick*, 1983; *Kong et al*., 1988; *Pockalny et al*., 1988; *Mével et al*., 1991; *Auzende et al*., 1994; *Cannat et al*., 1995; *Karson and Lawrence*, 1997a], augmented by our own interpretation based on seafloor morphology.

that this terrain represents ancient axial volcanic ridges that were dissected by faulting as they were transported off axis [*Karson and Dick*, 1983; *Pockalny et al*., 1988]. The inside corner, on the other hand, is characterized by very strong relief, with seafloor rising from the >6000 m deep nodal basin to a large topographic high (the RTI massif, summit at ~1000 mbsl; Figure 1). Dive observations have shown that the top of the RTI massif is comprised of basaltic rocks [*Mével et al*., 1991]. In contrast, below 2500 mbsl, the eastern face of the RTI massif exposes plutonic rocks. Structurally, the eastern face is characterized by abundant moderately east-dipping (~30–45°) faults, subparallel to the overall slope, with downdip slickensides [*Karson and Dick*, 1983; *Mével et al*., 1991]. In addition, the gabbroic rocks record a history of progressive down-temperature deformation, from magmatic through crystal plastic to brittle cataclastic, with a consistent normal shear sense [*Karson and Dick*, 1983; *Mével et al*., 1991; *Fletcher et al*., 1997]. These observations suggest that the slope surface is part of a detachment fault that has unroofed plutonic rocks formed beneath the ridge axis [*Dick et al*., 1981; *Karson and Dick*, 1983; *Mével et al*., 1991; *Karson and Lawrence*, 1997a]. The detachment is crosscut by small, steeper (~50–90°) east-dipping normal faults with offsets of typically a few tens of meters [*Karson and Dick*, 1983; *Mével et al*., 1991].

2.2. Leg 153 Gabbros

The gabbroic rocks exposed at the RTI massif were drilled during ODP Leg 153. Hole 923A, located at 23°32.556′N, 45°01.896′W (2429 mbsl), achieved the deepest penetration (70 m), recovering 41 m of core [*Cannat et al*., 1995]. This section is comprised of a diverse suite of predominantly fresh, texturally heterogeneous olivine gabbros, gabbros and troctolites, with subordinate gabbronorite, oxide gabbro, and rare leucocratic veins. These rocks are interlayered on centimeter to meter scale. The dominant lithologies are gabbros and olivine gabbros characterized by prominent brown cumulus clinopyroxene (referred to as brown-pyroxene gabbros) and olivine gabbros and troctolites with green, poikilitic clinopyroxene (poikilitic olivine gabbros). Modal and grain size layering is common, as is a magmatic foliation defined by shape-preferred orientations of cumulus plagioclase and pyroxene [*Cannat et al*., 1995]. This magmatic fabric is locally overprinted by a solid-state fabric, particularly close to the seafloor [*Cannat et al*., 1995]. Near the top of the hole (<20 mbsf), the brown-pyroxene gabbros contain rare intervals of oxide gabbros. Leucocratic veins, on the other hand, occur in the deeper part of the hole (>30 mbsf), and range in composition from plagioclase-rich gabbro to diorite (hornblende + plagioclase ± apatite).

Shipboard observations led to the subdivision of the section into five units, which predominantly represent alternating brown-pyroxene gabbros and poikilitic olivine gabbros [*Karson and Dick*, 1983]. Mineral zoning in major and trace elements, as well as the presence of trace phases (hornblende, apatite, ilmenite, zircon, and baddeleyite) in otherwise primitive rock, attests to a postcumulus history of porous melt migration within these units [*Casey*, 1997; *Ross and Elthon*, 1997; *Coogan et al*., 2000]. The oxide gabbros and leucocratic veins are considered to have formed by remobilization of such intercumulus melt [*Cannat et al*., 1995; *Casey*, 1997].

3. Reconstruction of Crystallization Depths

In this paper, we combine a tectonic reconstruction of the RTI with spreading rate data and U-Pb geochronology to calculate the crystallization depth of the gabbroic rocks drilled in Hole 923A. Our underlying rationale is that if the transport path, rate of transport, and age of a rock can be determined, its location of crystallization can be calculated. Below, we constrain each of these three input parameters.

3.1. Transport Path

The extensive geological and geophysical data available for the MARK area allow us to place constraints on the transport path that the rocks drilled in Hole 923A have taken to arrive at their current position. In order to do so, we derive a tectonic history for the RTI massif, focusing on a ridge-orthogonal cross section that runs through Hole 923A (Figure 2). This cross section runs from the top of the RTI massif in the west, along the eastern face of the RTI massif to the axial valley (including the Snake Pit AVR).

The plutonic rocks exposed at the eastern face of the RTI massif were emplaced in their current position as a result of movement on the detachment fault scarp that forms its eastern boundary [*Dick et al*., 1981; *Karson and Dick*, 1983; *Mével et al*., 1991; *Karson and Lawrence*, 1997a]; hence, their transport path must be a direct function of the geometry of the detachment fault. To the northeast of Hole 923A, the exposure of plutonic rocks on the seafloor extends to depth of at least 6000 mbsl, well into the nodal basin [*Mével et al*., 1991]. South of this, downslope of Hole 923A, basaltic rocks are exposed, with the gabbro-basalt contact occurring around

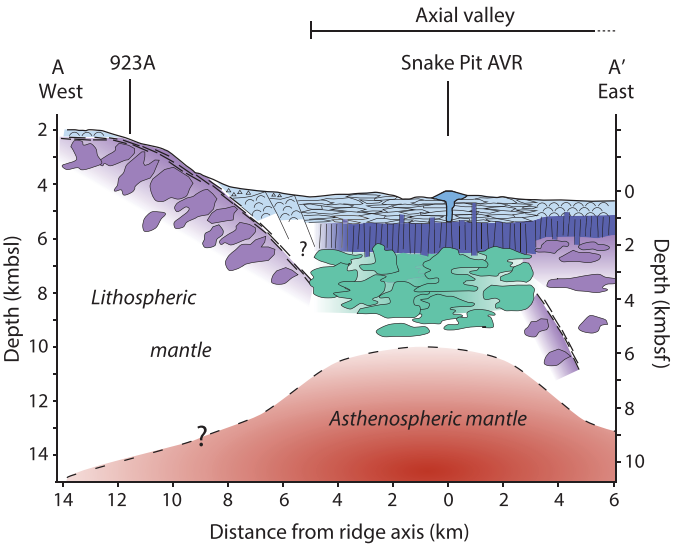

Figure 2. Interpretative cross section (no vertical exaggeration) across the ridge axis and the eastern face of the RTI massif (see Figure 1 for location). Geometry of the detachment fault is constrained at the surface [*Karson and Dick*, 1983], and subsurface extension is inferred from various other constraints (geological, microearthquake, and paleomagnetic data and modeling; see text for discussion). Crustal thickness beneath the neovolcanic zone is constrained by seismic data to be ~4–5 km [*Detrick and Purdy*, 1980; *Purdy and Detrick*, 1986]. The thickness of the gabbroic section beneath the detachment is unknown, but based on the exposure of peridotites along the detachment just south of the map area [*Mével et al.*, 1991; *Karson and Lawrence*, 1997b], we infer that the plutonic section is relatively thin, and partially intercalated with peridotites [cf. *Cannat*, 1996]. Crust formed during detachment-dominated spreading is distinguished from crust formed during magmatically dominated spreading by the color of the plutonic sections (purple and green, respectively).

3250 mbsl [*Karson and Dick*, 1983; *Mével et al.*, 1991]. These relationships indicate that the detachment fault is extensive, and that it continues subsurface below the basaltic rocks downslope of Hole 923A [*Karson and Lawrence*, 1997a]. The basaltic rocks (between 5 and 8 km along western half of the profile; Figure 2) occur along the northern end of a large (~10 × 4 km) massif, which forms a distinct morphological unit rising 1200 m from the axial valley floor (Figure 1). This plateau has an apparently fault-bounded, lobate eastern margin, disrupting the north-south orientation of the axial valley wall. Based on its size, elevation above the axial valley floor and the observation that it disrupts the axial valley wall, we infer this plateau to be a fault klippe, and that it forms the hanging wall to the detachment fault plane exposed upslope.

The presence of a well-defined, hydrothermally active axial volcanic ridge (Snake Pit AVR) comprised of basaltic flows with fresh glass and little sediment cover [*Brown and Karson*, 1988; *Kong et al.*, 1988; *Gente et al.*, 1991], underlain by relatively thick crust containing partial melt [*Canales et al.*, 2000], indicates that the northern MARK segment is currently in a predominantly magmatic mode of crustal accretion. The rift valley floor adjacent to the Snake Pit AVR is comprised of basaltic lavas covered by sediment. Sediment thickness increases stepwise away from the ridge axis, and these abrupt increases in sediment thickness occur at the flow fronts of younger lava flows on older, more sedimented flows [*Gente et al.*, 1991]; hence, the axial valley floor records a history of successive episodes of volcanic accretion, with the Snake Pit AVR being the most recent. Within the E-W profile that contains Hole 923A (23°32′N), these basalts extend to 5.1 km west of the ridge axis (Figures 1 and 2). Here a marked break in slope is present, which marks the contact between the constructional volcanic terrain of the rift valley and the basalts inferred to comprise the hanging wall block to the detachment (Figure 2). Hence, it represents the location where magmatically dominated spreading (the constructional terrain of the axial valley floor) superseded detachment-dominated spreading. We contend that this contact marks a renewal of magmatism that cutoff the detachment after it unroofed the plutonic rocks along the eastern slope of the RTI [cf. *Tucholke et al.*, 1998; *MacLeod et al.*, 2009], and hence that it marks the time at which the detachment fault ceased to be active. This is supported by seismic tomography data of the northern MARK segment at 23°20′N, which show the lower crustal low-velocity zone beneath the Snake Pit AVR extending west by ~4 km, to directly beneath the fault scarp defining the western wall of the axial valley, where peridotites are exposed [*Canales et al.*, 2000]. The contact between the low and high-velocity domains is abrupt and subvertical [*Canales et al.*, 2000]. These data indicate that the entire central and western portion of the axial valley is underlain by a magmatic system, and that this system superseded the faults that exhumed the mantle rocks on the western axial valley wall. We assume that this is also the case just to the north, where the basaltic axial valley floor extends to 5.1 km west of the ridge axis. This implies that the rocks drilled in Hole 923A have been carried off axis passively for 5.1 km.

The final piece of information required to reconstruct the transport path of the gabbros is the geometry of the detachment fault. From seafloor observations, *Karson and Dick* [1983] determined a dip of 30° for the

exposed part of the fault, arguing that the eastern face of the RTI massif is the dip slope of the detachment. However, these observations do not constrain the geometry at depth. Both seafloor [*MacLeod et al*., 2009] and seismic [*Ranero and Reston*, 1999] observations have shown that oceanic detachment faults are typically characterized by a convex-upward geometry, with the fault steepening toward the ridge axis. In addition, *MacLeod et al*. [2009] demonstrated that the detachment fault at the 13°20′N core complex on the Mid-Atlantic Ridge has a constant change in slope (i.e., constant curvature) in its exposed portion. Such geometry is consistent with numerical models of faulting at spreading ridges, which also predict convex-upward detachments [*Lavier et al*., 1999; *Buck et al*., 2005]. *MacLeod et al*. [2009] further determined an initial subsurface dip of 65 $\pm$ 10° for the three detachment faults at 13°N on the MAR by analyzing the geometry of tilted volcanic surfaces and their associated faults. This calculated dip is consistent with the 70° dip of the TAG detachment at its initiation 7 km subsurface, as indicated by microearthquakes [*deMartin et al*., 2007]. Paleomagnetic data can also be used to constrain the degree of footwall rotation below the Curie temperature (~550°C). The inferred footwall rotation calculated using paleomagnetic data from the core complexes at 15°45′N (64 $\pm$ 16°) [*MacLeod et al*., 2011] and Atlantis Massif (46 $\pm$ 6°) [*Morris et al*., 2009] are consistent with a convex-upward geometry as well as the inferred initial dips of the TAG and 13°N detachment faults.

On the basis of these data, we initially assume that, in the MARK area, the detachment fault dips 30° at the surface in the vicinity of Hole 923A (as observed) [*Karson and Dick*, 1983], and that it has a convex-upward geometry with a constant curvature and dip of 65° at 7 km depth. In such a scenario, the detachment fault can be described as part of a circle with a radius of 20.2 km. We explore the effect of uncertainties in this geometry in the discussion (section 4.1). We further note that this assumption only defines the radius of curvature of the fault; it does not prescribe the depth to which the fault extends.

3.2. Spreading Rate Versus Slip Rate

The spreading history of the MARK area has been constrained by a number of magnetic anomaly studies [*Schulz et al*., 1988; *Gente et al*., 1995; *Williams*, 2007]. *Schulz et al*. [1988] found a full spreading rate 25.4 mm/yr for the MARK area, with 14.1 mm/yr accommodated by the American plate and 11.3 mm/yr by the African plate. More recently, *Williams* [2007] made a detailed analysis of the spreading history of the northern spreading segment (including the RTI massif) along three profiles, and found a 23.4 mm/yr full spreading rate, with 14.4 mm/yr to the west and 9.0 mm/yr to the east. It is these rates, utilized also by *Dick et al*. [2008], that are used in this paper; we consider the *Williams* [2007] study to be the most relevant, because it explicitly focused on the relatively recent (<10 Ma) evolution of the American plate in the study area and hence provides the best available constraints for the time window being considered here.

These rates define the asymmetry in spreading across the northern MARK segment to be 61.5% (50% being symmetrical spreading). This asymmetry represents a long-term (10 Ma) average, and includes periods of increased asymmetry (up to 78%) during formation of oceanic core complexes, with either low or no asymmetry in the intervening periods [*Williams*, 2007, Figure 4.6]. The asymmetry found during core complex formation in the MARK area is in line with spreading asymmetries documented for other detachment-dominated segments. *Searle et al*. [2003] determined 77% asymmetry at the FUJI Dome on the Southwest Indian Ridge from sea surface magnetic data. *Okino et al*. [2004] found a similar asymmetry (75%) at the Australian-Antarctic Discordance. *Baines et al*. [2008] and *Grimes et al*. [2008] used age-distance regressions provided by U-Pb zircon dates to calculate spreading rates for Atlantis Bank (57°E, Southwest Indian Ridge) and Atlantis Massif (30°N, Mid-Atlantic Ridge), and found 80% and 100% asymmetry, respectively.

We use the spreading rate as recorded on the American plate to estimate the slip rate on the detachment fault. The high degrees of spreading asymmetry observed both in the MARK area and in detachment-dominated segments elsewhere (as discussed above) imply that detachment faults preferentially accommodate spreading. Asymmetry is probably a consequence of the acceleration of slip rates on the detachment faults as strain is localized onto them as weak phyllosilicates (e.g., talc) form along the fault planes [*MacLeod et al*., 2002]; ultimately slip may exceed the long-term half-spreading rate [*Baines et al*., 2008; *Grimes et al*., 2008], and the detachment faults accommodate all of the spreading on the side of the ridge on which they occur. The detachment faults therefore tend to form what is effectively the plate boundary along which spreading is accommodated [*Allerton et al*., 2000; *Baines et al*., 2008; *Grimes et al*., 2008; *MacLeod et al*., 2009]. It follows that the slip rate on the detachment faults can be related directly to the spreading rate on the side of the ridge on which the detachment is located. Moreover, because detachment faults likely rotate

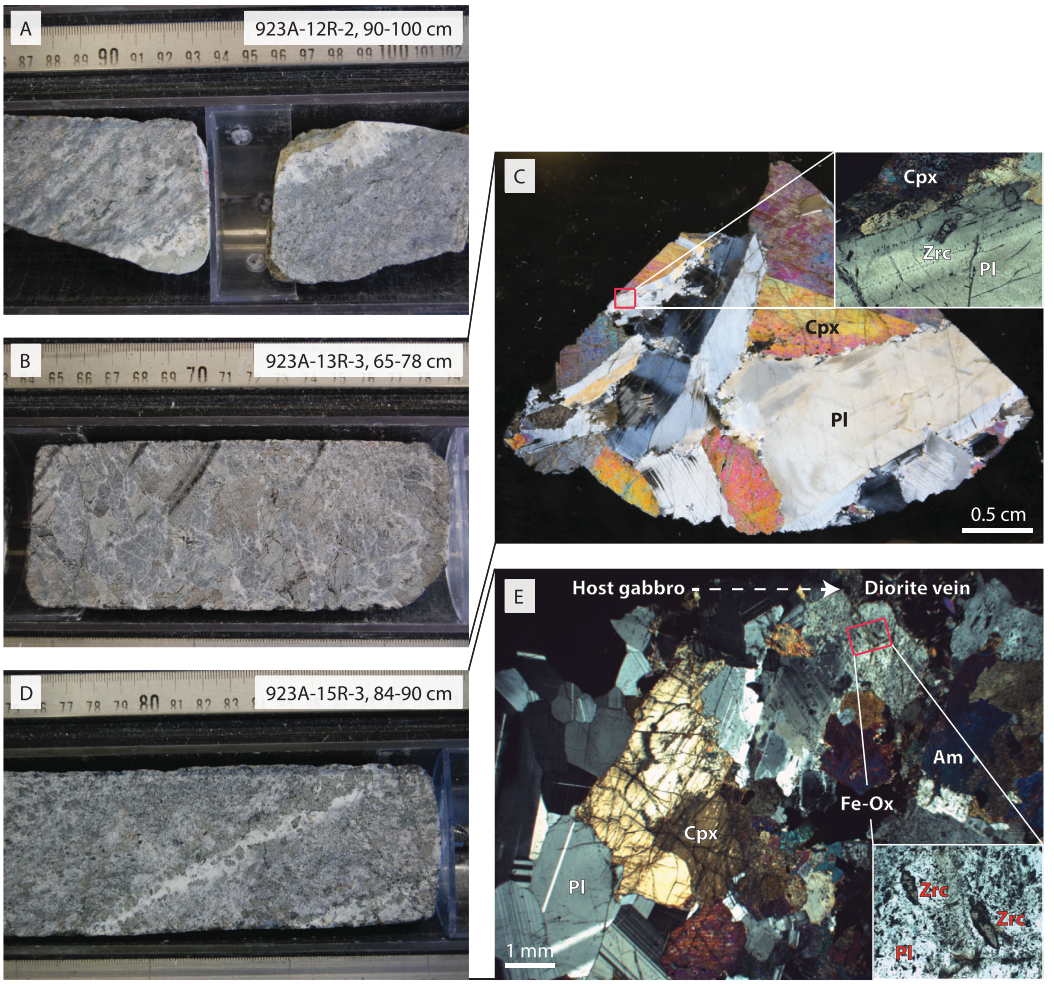

Figure 3. Sample photographs and photomicrographs of the three samples dated in this study. (a) Diorite vein crosscutting gabbroic rocks of Unit 4 (Sample 923A-12R-2, 90–100 cm; 48 mbsf). No thin section is available for this sample due to limited amount of material; (b) very coarse-grained orthopyroxene and oxide-bearing gabbro from Unit 4 (sample 923A-13R-3, 65–78 cm; 54 mbsf); (c) photomicrograph of sample 923A-13R-3, 65–78 cm, illustrating the granular igneous texture of the sample and the minor deformation overprint along plagioclase grain boundaries. Inset shows zircon occurring as inclusions in the undeformed portions of the igneous plagioclase. (d) Diorite vein crosscutting poikilitic olivine gabbros from Unit 5 (sample 923A-15R-3, 84–90 cm; 64 mbsf). (e) Photomicrograph of sample 923A-15R-3, 84–90 cm, illustrating the vein and its diffuse contact with the host gabbro, as well as the occurrence of zircon as inclusions in vein plagioclase (inset). Am = amphibole; Cpx = clinopyroxene; Fe-Ox = iron oxide; Pl = plagioclase; Zrc = zircon.

from high angles at depth to shallow angles at the surface due to flexural rotation, the slip rate of the exposed, shallow part of detachment faults equals the slip rate on the deeper, steep sections of the fault [*Baines et al.*, 2008]. On the basis of these constraints, we assume that the detachment fault that exposed the plutonic rocks on the eastern face of the MARK RTI massif took up all of the spreading on the western side of the ridge axis when it was active, slipping by 14.4 mm/yr.

3.3. Ages From U-Pb Geochronology

We sampled core recovered from ODP Hole 923A at the IODP core repository in Bremen, and selected three intervals for U-Pb zircon geochronology (Figure 3). Sample 923A-12R-2, 90–100 cm (48 mbsf) is a 1–1.5 cm wide, coarse-grained dioritic vein composed of plagioclase, hornblende, and Fe-Ti oxide with accessory apatite and zircon, which crosscuts deformed brown-pyroxene gabbros of Unit 4 (Figure 3a). The contact is moderately sharp. Sample 923A-13R-3, 65–78 cm (54 mbsf) is representative of its host rock; it is a very coarse grained (grain size ~2 cm) gabbro with minor orthopyroxene and interstitial Fe-Ti oxides (Figures 3b and 3c), and forms part of the modally and grain-size graded brown-pyroxene gabbro facies that constitute Unit 4. The gabbro largely retains a granular igneous texture, but records minor solid-state deformation in the form of recrystallization along the rims of igneous plagioclase (Figure 3c). In thin section, zircon occurs as inclusions within the undeformed portions of

plagioclase (Figure 3c, inset): hence, the dated zircon most likely formed during crystallization of the gabbro, and predated the deformation of the host plagioclase. Sample 923A-15R-3, 84–90 cm (64 mbsf) is a ~0.5 cm wide dioritic vein that crosscuts poikilitic olivine gabbros of Unit 5 (Figures 3d and 3e). The contact with the host gabbro is diffuse, and the vein incorporates grains from the host gabbro. It is composed of plagioclase, hornblende, Fe-Ti oxides, and epidote. Accessory zircon occurs as inclusions in plagioclase within the vein (Figure 3e).

Zircons were separated from these samples for U-Pb geochronology. Single grain and grain-fragment U-Pb zircon dates were determined by isotope dilution-thermal ionization mass spectrometry (ID-TIMS) at the Massachusetts Institute of Technology. Zircons were dissolved following the chemical abrasion procedure [*Mattinson*, 2005] modified for single grains as described in *Lissenberg et al*. [2009] and *Rioux et al*. [2012]. Data were reduced using the ET_redux software package [*Bowring et al*., 2011; *McLean et al*., 2011], with parameters outlined in *Rioux et al*. [2015a]. $^{206}Pb/^{238}U$ dates were corrected for initial ^{230}Th disequilibrium using an assumed melt Th/U based on a global average of MORB glasses (Th/U = 2.63 ± 0.90), following *Rioux et al*. [2015a]. All dates discussed in this manuscript are Th-corrected $^{206}Pb/^{238}U$ dates. Two low-precision dates (fractions 923A-15R-3, 84–90 cm z3 and 923A-12R-2, 90–100 cm z3-2) are excluded from the data plots and the discussion below; the dates from these fractions overlap the rest of the reported dates, but have relatively large analytical uncertainties due to low radiogenic Pb to common Pb ratios (Pb^*/Pb_c). We note that it is unlikely that the zircons were impacted by substantial Pb loss, given their low U contents, young age, and the pretreatment using the chemical abrasion method [*Mattinson*, 2005].

U-Pb geochronology results are provided in Table 1 and illustrated in Figures 4 and 5. Single grain uncertainties throughout are ±2σ internal and weighted mean uncertainties are ±2σ internal/external, where the external uncertainties include the analytical uncertainties, uncertainties in the tracer calibration [*McLean et al*., 2011, 2015; Condon et al., 2015], and uncertainties in the ^{238}U decay constant (±0.017%) [*Jaffey et al*., 1971]. Samples 923A-13R-3, 65–78 cm and 923A-15R-3, 84–90 cm yielded ranges of dates of 1.153 ± 0.043 to 1.213 ± 0.021 and 1.138 ± 0.062 to 1.198 ± 0.030 Ma, respectively. A single precise analysis for 923A-12R-2, 90–100 cm yielded a date of 1.169 ± 0.043 Ma. The range of single grain dates in each sample overlap; however, there is a small offset between the weighted mean $^{206}Pb/^{238}U$ dates for samples 923A-13R-3, 65–78 cm (1.194 ± 0.015/0.019 Ma; mean square of weighted deviates; MSWD = 2.03) and 923A-15R-3, 84–90 cm (1.165 ± 0.012/0.014 Ma; MSWD = 2.31). The MSWDs of the weighted means are within the 95% confidence interval of the expected MSWD for a single population.

Two possible interpretations of the dates are (Figure 4): (1) the intrasample variability in samples 923A-13R-3, 65–78 cm and 923A-15R-3, 84–90 cm reflects analytical scatter about the true crystallization ages of each of the magmas. The weighted mean dates are then the most accurate estimates of the crystallization ages, suggesting an age difference of 0.030 ± 0.019 Ma between the two samples. (2) The slightly elevated MSWDs for the weighted mean dates reflect true variability in zircon crystallization dates within the samples. This latter interpretation is consistent with previous zircon dating studies of oceanic gabbros, which have shown that these rocks may contain a range of zircon dates as a result of either prolonged zircon crystallization or inheritance of older zircon [*Schwartz et al*., 2005; *Lissenberg et al*., 2009; *Rioux et al*., 2012, 2015b]. In this case, the range of dates from each sample overlap and the magmas may have been coeval; the offset weighted mean dates may reflect the small sample sizes and distribution of precise analyses, where the weighted mean for 923A-13R-3, 65–78 cm is skewed to an older age by a single precise older date (z6). If there is real scatter in the zircon dates, calculated weighted mean dates excluding the potentially inherited older grains in each sample would provide the best estimate of the final crystallization of the magmas (model 2 in Figure 4). The combined data of the younger fractions from all three samples yield a weighted mean $^{206}Pb/^{238}U$ date of 1.164 ± 0.011/0.014 (MSWD = 0.83; Figure 5).

It is not possible to distinguish between the two interpretations of the U-Pb dates based on the current data set; however, the crystallization depths calculated here are insensitive to the chosen model. For convenience, we adopt the combined weighted mean date of 1.164 ± 0.011/0.014 Ma as the best estimate of the crystallization age of the samples. If we instead use the individual weighted mean dates from 923A-13R-3, 65–78 cm and 923A-15R-3, 84–90 cm, the calculated crystallization depths vary by <0.4 km (see section 4.1.4)

3.4. Crystallization Depth

The tectonic constraints, spreading rate data and zircon dates can be integrated to yield a complete model for the transport history for the gabbros recovered from Hole 923A (Figure 6). We discuss this history in reverse order, starting at the present day, to arrive at the crystallization depths of the samples.

Table 1. ID-TIMS Zircon Data

	923A-12R-2, 90–100 cm; diorite			923A-13R-3, 65–78 cm; gabbro					923A-15R-3, 84–90 cm; diorite				
	z2-2	z3-2	z4-2	z5	z6	z7	z8	z1-2	z2-2	z3	z4	z5	z7
Pb*/Pbc[a]	0.29	0.13	0.22	0.35	0.62	0.43	0.22	0.49	0.18	0.08	0.56	0.66	0.47
Pb* (pg)[b]	0.18	0.14	0.13	0.07	0.11	0.07	0.04	0.27	0.17	0.06	0.11	0.12	0.25
Pbc (pg)[b]	0.64	1.08	0.57	0.18	0.18	0.17	0.17	0.55	0.95	0.80	0.19	0.19	0.53
Th/U[c]	0.394	0.404	0.377	0.480	0.260	0.390	0.268	0.463	0.278	0.126	0.222	0.271	0.566
$^{206}Pb/^{204}Pb$[d]	35.99	25.97	31.89	39.19	57.63	44.69	32.39	47.37	29.69	23.52	54.43	60.36	45.52
$^{208}Pb/^{206}Pb$[d]	0.137	0.139	0.131	0.167	0.091	0.135	0.094	0.160	0.097	0.045	0.078	0.095	0.195
Uncorrected													
$^{206}Pb/^{238}U$[e]	0.0001670	0.0001829	0.0001672	0.0001650	0.0001729	0.0001693	0.0001685	0.0001692	0.0001614	0.0001530	0.0001631	0.0001643	0.0001726
±2σ%	4.27	9.94	5.66	4.48	2.04	3.03	5.61	2.78	6.43	14.46	2.12	2.35	2.78
$^{207}Pb/^{235}U$[e]	0.00109	0.00201	0.00120	0.00149	0.00116	0.00109	0.00116	0.00155	0.00092	0.00085	0.00102	0.00103	0.00175
±2σ%	63.4	83.0	75.2	52.2	28.4	44.6	76.9	30.0	103.4	237.8	32.9	36.0	25.2
$^{207}Pb/^{206}Pb$[e]	0.047	0.080	0.052	0.066	0.049	0.047	0.050	0.067	0.042	0.040	0.045	0.046	0.074
±2σ%	62.1	80.2	73.3	49.6	27.6	43.5	74.9	28.9	101.7	233.7	32.1	34.6	24.4
rho[f]	0.334	0.336	0.368	0.593	0.405	0.410	0.402	0.429	0.283	0.310	0.374	0.616	0.337
$^{206}Pb/^{238}U$ date[g]	1.077	1.179	1.078	1.064	1.114	1.091	1.086	1.091	1.041	0.986	1.051	1.059	1.113
±2σ abs	0.046	0.117	0.061	0.048	0.023	0.033	0.061	0.030	0.067	0.143	0.022	0.025	0.031
$^{207}Pb/^{235}U$ date[g]	1.10	2.04	1.22	1.52	1.18	1.10	1.18	1.58	0.94	0.86	1.04	1.05	1.78
±2σ abs	0.70	1.69	0.92	0.79	0.33	0.49	0.91	0.47	0.97	2.05	0.34	0.38	0.45
$^{207}Pb/^{206}Pb$ date[g]	59	1193	291	795	134	29	198	824	−254	−337	−35	−25	1034
±2σ abs	1480	1583	1675	1041	650	1042	1739	603	2576	6017	780	837	493
% discordance[h]	98.2	99.9	99.6	99.9	99.2	96.3	99.5	99.9	100.4	100.3	103.0	104.3	99.9
Th Corrected													
$^{206}Pb/^{238}U$[e]	0.0001814	0.0001972	0.0001817	0.0001788	0.0001881	0.0001837	0.0001837	0.0001832	0.0001766	0.0001691	0.0001786	0.0001795	0.0001859
±2σ%	3.65	8.53	4.78	3.70	1.72	2.58	4.67	2.40	5.42	11.90	1.78	1.90	2.49
$^{207}Pb/^{206}Pb$[e]	0.043	0.074	0.048	0.061	0.045	0.043	0.046	0.062	0.038	0.036	0.041	0.042	0.068
±2σ%	62.6	81.2	74.0	50.4	27.9	43.9	75.6	29.3	102.4	235.5	32.4	35.0	24.7
rho[f]	0.246	0.259	0.278	0.503	0.316	0.317	0.316	0.325	0.196	0.219	0.281	0.532	0.245
$^{206}Pb/^{238}U$ date[g]	1.169	1.271	1.171	1.153	1.213	1.184	1.184	1.181	1.138	1.090	1.151	1.157	1.198
±2σ abs	0.043	0.108	0.056	0.043	0.021	0.031	0.055	0.028	0.062	0.130	0.021	0.022	0.030
$^{207}Pb/^{206}Pb$ date[g]	−142	1043	97	624	−68	−171	−7	656	−486	−602	−260	−243	883
±2σ abs	1550	1639	1752	1087	681	1093	1825	628	2719	6403	822	884	511
% discordance[h]	100.8	99.9	98.8	99.8	101.8	100.7	117.0	99.8	100.2	100.2	100.4	100.5	99.9

[a]Ratio of radiogenic to common Pb.
[b]Total radiogenic Pb, common Pb, and U (picograms).
[c]Th/U ratio calculated from $^{208}Pb/^{206}Pb$ and the $^{206}Pb/^{238}U$ date of the fraction.
[d]Fractionation and spike-corrected isotopic ratios, reduced using EARTHTIME ET535 tracer calibration v.3.
[e]Fractionation, spike, and blank-corrected radiogenic isotope ratios. Laboratory blanks were corrected using $^{206}Pb/^{204}Pb = 18.638 \pm 0.707$, $^{207}Pb/^{204}Pb = 15.494 \pm 0.449$, $^{208}Pb/^{204}Pb = 37.748 \pm 1.227$.
[f]Correlation coefficient of radiogenic $^{207}Pb^*/^{235}U$ and $^{206}Pb^*/^{238}U$.
[g]Dates (Ma) calculated using $^{238}U/^{235}U = 137.818$ [*Hiess et al.*, 2012], and decay constants of $^{238}U = 1.5513 \times 10^{-10}$ yr^{-1} and $^{235}U = 9.8485 \times 10^{-10}$ yr^{-1} [*Jaffey et al.*, 1971].
[h]% discordance = 100 − (100 × ($^{206}Pb/^{238}U$ date)/($^{207}Pb/^{206}Pb$ date)).

Currently, the northern segment in the MARK area is spreading magmatically, as indicated by both seismic and geological observations on the Snake Pit AVR [*Karson and Brown*, 1988; *Kong et al.*, 1988; *Gente et al.*, 1991; *Canales et al.*, 2000; *Sturm et al.*, 2000]. The rift valley floor to the west of the Snake Pit AVR consists of successively older volcanic rocks [*Gente et al.*, 1991], which extend to 5.1 km west of the ridge axis in the section examined here. Given the half-spreading rate of 14.4 km/Ma, this indicates that the northern spreading segment has accommodated magmatic accretion for the last 0.354 Ma; this calculated age for the tectonic to magmatic spreading transition is very close to that of 0.4 Ma estimated by *Canales et al.* [2000] based on seismic data. During this time, the rocks sampled in Hole 923A were carried off axis passively, having already been uplifted to their current structural configuration.

Prior to this time, the detachment fault was active. The duration of the detachment faulting responsible for emplacement of the sampled rocks is given by the mean U-Pb zircon date (1.176 Ma) minus the period of spreading after the detachment fault had been cutoff (0.354 Ma). This constrains the duration of detachment faulting to be 0.822 Ma. The distance the rocks have been transported along the detachment, then, is given by multiplying this duration by the slip rate. As discussed above, we assume that all of the spreading on the western side of the ridge axis (i.e., the American plate) was accommodated by detachment faulting, which provides a slip rate of 14.4 km/Ma [*Williams*, 2007]. Making this assumption, the sampled rocks have traveled 11.66 km along the detachment fault. With the detachment fault geometry defined as a circle with

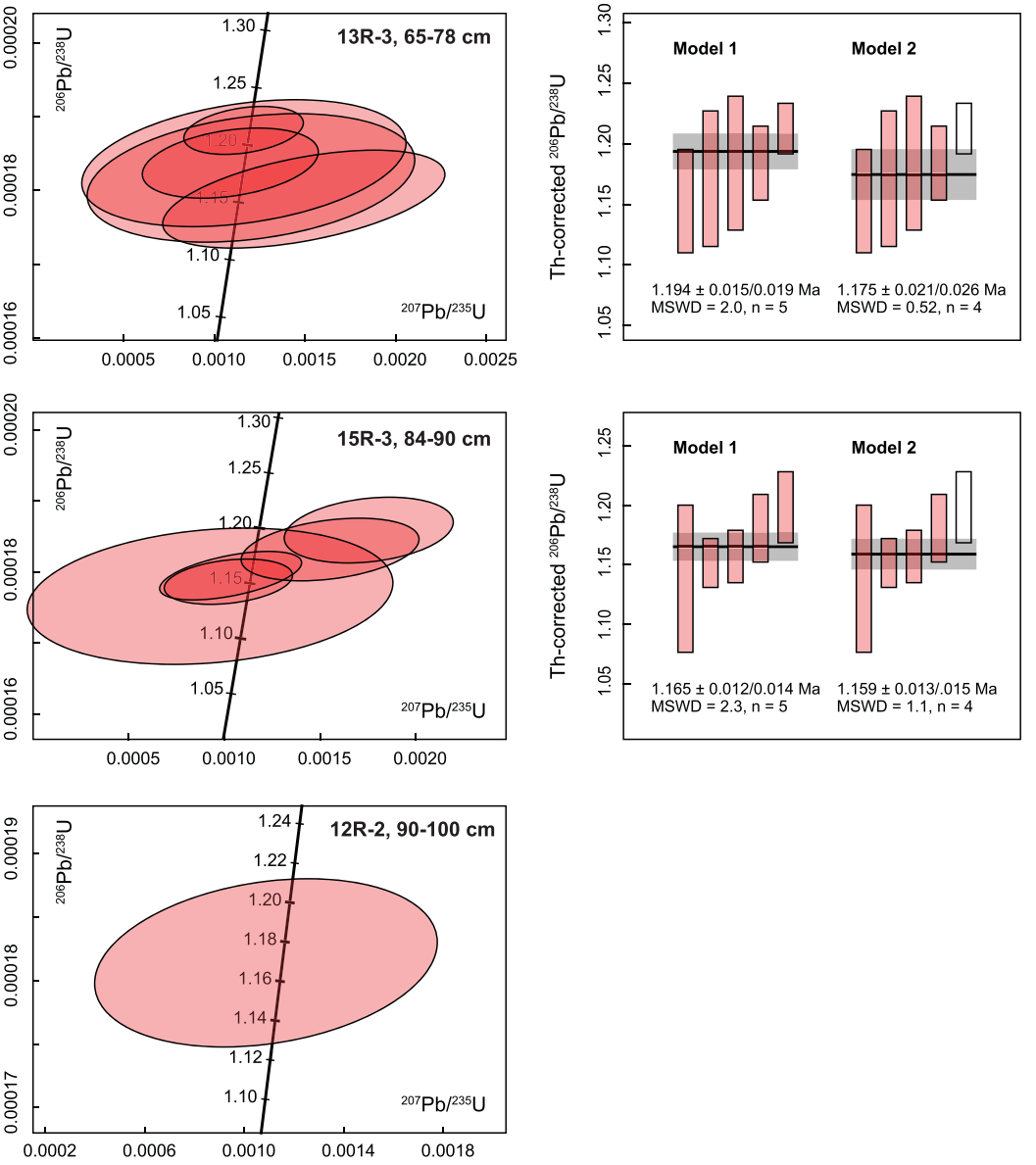

Figure 4. U-Pb concordia diagrams and weighted mean $^{206}Pb/^{238}U$ plots of single-grain and grain fragment zircon dates. All data are corrected for initial ^{230}Th exclusion as described in the text. Ages on concordia are in Ma. Plots and weighted mean calculations were generated using the U-Pb_redux software package [*Bowring et al.*, 2011; *McLean et al.*, 2011]. The weighted mean plots include the weighted mean of the entire data set (model 1) and the weighted mean excluding the oldest date (model 2). Data from fractions 15-3 z3 and 12-8A z3-2 are excluded from the plots for clarity.

a radius of 20.2 km (see section 3.1), this yields a depth of crystallization of 6.4 km beneath the seafloor (Figure 6). The uncertainties that are clearly inherent in these calculations are discussed in detail in turn below.

4. Evaluation of Uncertainties

Our reconstruction has allowed us to calculate the crystallization depth of magmas beneath the detachment-dominated northern MARK segment to be 6.4 km. This calculation is subject to a number of uncertainties, which we discuss here.

4.1. Detachment Fault Geometry

The geometry of the detachment fault plays a critical role in the calculation of the crystallization depth. It is important, therefore, to assess the effect of the assumed geometry on the depths. In this section, we

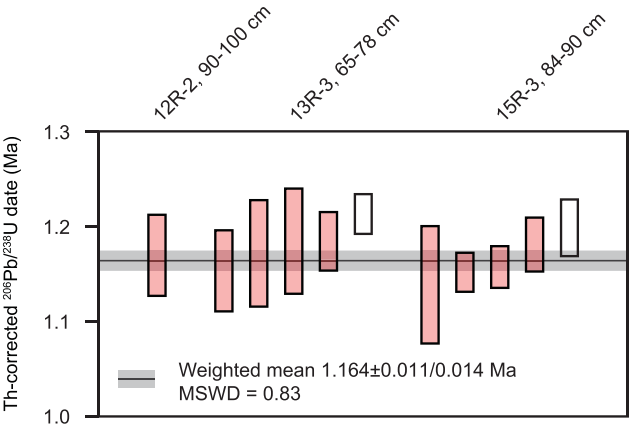

Figure 5. Th-corrected $^{206}Pb/^{238}U$ dates for the full zircon population analyzed. White bars represent grains not included calculation of weighted mean date (see text for discussion).

evaluate a range of detachment fault geometries, and discuss the uncertainty in crystallization depth that results from these.

On the basis of seafloor observations [*MacLeod et al.*, 2009], paleomagnetic evidence for footwall rotation [*Morris et al.*, 2009; *MacLeod et al.*, 2011], as well as geophysical data [*Ranero and Reston*, 1999; *deMartin et al.*, 2007] and "rolling hinge" numerical models [*Lavier et al.*, 1999; *Buck et al.*, 2005], we have assumed a convex-upward geometry for the detachment fault. We consider this assumption to be robust. However, the degree of curvature is difficult to ascertain. In our initial reconstruction, above, we assume constant curvature with a 65° dip at 7 km depth on the basis of core complexes at 13°N on the Mid-Atlantic Ridge [*MacLeod et al.*, 2009]. This primary dip is subject to an uncertainty of ±10°, which represents the standard deviation of the mean reconstructed fault dip [*MacLeod et al.*, 2009]. Hence, we have calculated crystallization depths assuming initial dips of 55° and 75°, and find values of 5.6 and 7.1 km, respectively (Table 2). An initial fault dip of 65 ± 10° thus leads to a crystallization depth of 6.4 ± 0.8 km. We have also examined the most extreme initial dips for curved detachments allowed by the paleomagnetic constraints on footwall rotation at Mid-Atlantic Ridge detachments [*Morris et al.*, 2009; *MacLeod et al.*, 2011]. Since the sampled rocks of these studies were taken from the approximately horizontal parts of the detachment faults, their footwall rotations of 64 ± 16° [*MacLeod et al.*, 2011] and 46 ± 6° [*Morris et al.*, 2009] translate into initial dips of the same magnitude at the time the footwalls cooled below the Curie temperature. Hence, we have calculated crystallization depths for initial dips of 40° (the minimum subsurface dip as defined by the 46 ± 6° rotation of the Atlantis Massif detachment) and 80° (the maximum subsurface dip as defined by the 64 ± 16° rotation of the 15°N detachments). The results (Table 2) indicate crystallization depths of 4.6 and 7.4 km below seafloor, respectively. A final geometry examined (Figure 7) is that of the TAG detachment, which is characterized by a gently dipping, planar upper section (here taken as 30° based on seafloor observations of a 30° dip of the MARK RTI massif detachment at the surface) [*Karson and Dick*, 1983] and deeper section with a constant slope of 70° [*deMartin et al.*, 2007]. In this scenario, the crystallization depth

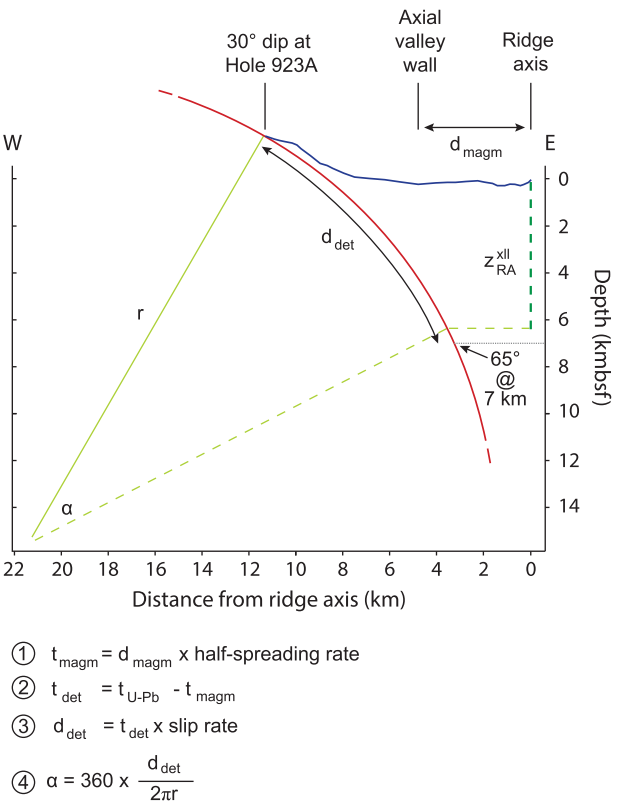

Figure 6. Cross section (no vertical exaggeration) showing method for calculating the crystallization depth Z^{xll}_{RA} for a convex-up detachment fault. The dip of the detachment fault at Hole 923A and 7 km subsurface define a circle with radius r. After subtraction of distance d_{magm} and hence duration t_{magm} of post-detachment spreading, the duration t_{det} and distance d_{det} of spreading on the detachment fault can be calculated using the weighted mean U-Pb zircon date $t_{U\text{-}Pb}$ and the slip rate. Following calculation of α, the crystallization depth beneath the ridge axis can be read off of the cross section.

Table 2. Crystallization Depths for Various Detachment Fault Geometries

Dip at Surface (°)	Dip at Depth (°)	Geometry	Crystallization Depth (km)
30	65	Convex-up, constant curvature	6.4
30	55	Convex-up, constant curvature	5.6
30	75	Convex-up, constant curvature	7.1
30	40	Convex-up, constant curvature	4.6
30	80	Convex-up, constant curvature	7.4
30	70	TAG; shallowly dipping planar upper section, steeply dipping planar deep section	6.1

can be calculated using trigonometry (see Figure 7), and amounts to 6.1 km (Table 2).

If the initial detachment dips were shallow (≤40°) in the subsurface, it would require that the Hole 923A gabbros crystallized on the opposite (i.e., eastern) side of the ridge, significantly offset from the spreading axis. A geometrical reconstruction of the location of crystallization relative to the ridge axis, further developed in section 4.2.1 below and illustrated in Figure 8, predicts that crystallization would be ~3.2 km east of the ridge axis for an initial dip of 40°. For shallower fault dips, this would increase further. We consider this to be unlikely. Furthermore, shallow melt emplacement is difficult to reconcile with the inferred thermal structure of detachment-dominated ridge segments on the Mid-Atlantic Ridge. Constraints on the thermal structure come from microearthquakes, which track the depth extent of the brittle part of the lithosphere, and from thermal models. Microearthquakes, and hence brittle deformation, extend to ~7 km depth at the TAG detachment (26°N, Mid-Atlantic Ridge) [*deMartin et al.*, 2007], indicating a cool thermal structure. This is consistent with findings from thermal models of detachment faults, which place the 600°C isotherm at ~5–6 km depth [*Grimes et al.*, 2011; *Schoolmeesters et al.*, 2012]. Hence, although we cannot completely rule out shallow (≤4.6 km), off-axis crystallization implied by models with shallow initial fault dips, available constraints suggests that this is unlikely, and we consider 6.4 ± 0.8 km (based on an initial dip of 65 ± 10°) to be the best estimate of the crystallization depth. We note that this estimate also covers the crystallization depth for a TAG-like geometry (6.1 km; Table 2).

4.2. Postdetachment Spreading

We have taken the time at which the detachment fault was cut off by renewed magmatism to be 0.354 Ma, interpreting the axial valley floor to be seafloor constructed postdetachment [cf. *Canales et al.*, 2000]. We cannot completely rule out that the older axial valley floor basalts west of the Snake Pit AVR represent stranded blocks of hanging wall to the detachment. If so, only the Snake Pit AVR itself would represent postdetachment, magmatically dominated accretion. Since the Snake Pit AVR extends 1.5 km to the west of the ridge axis in the section considered here, this would correspond to a time interval of 0.104 Ma. The remaining 1.072 Ma of spreading would then have been taken up by detachment faulting, leading to a crystallization depth of 9.8 km. However, this scenario would be difficult to reconcile with seismic data showing that the lower crustal low-velocity zone beneath the Snake Pit AVR extends to beneath the western fault scarp that exposes peridotites at 23°20′N [*Canales et al.*, 2000], covering the entire central and western portion of the axial valley. Furthermore, it would be at odds with the apparently continuous volcanic history of the axial valley, as inferred from the observation of stepwise

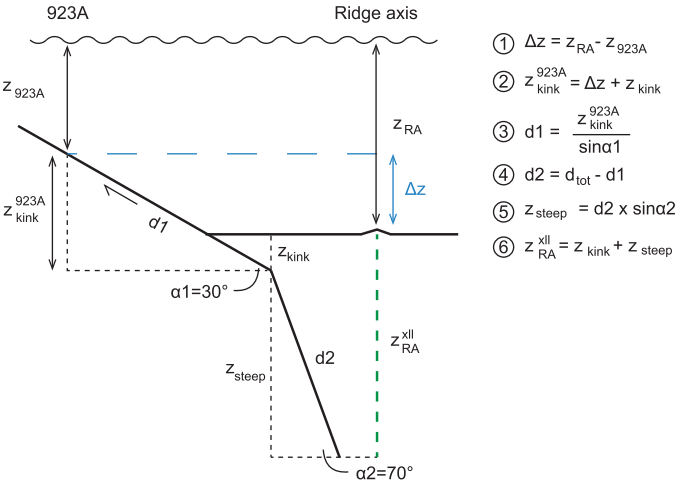

Figure 7. Schematic representation of the calculation of the crystallization depth Z^{xII}_{RA} for a detachment fault with a geometry similar to that at TAG [*deMartin et al.*, 2007], with a shallow upper section (30°, as constrained by seafloor observations) [*Karson and Dick*, 1983; *Karson and Lawrence*, 1997a] and a steeper deep section (70°, as at TAG). Z_{923A} is the water depth of Hole 923A (2429 mbsl), Z_{RA} is the water depth of the ridge axis (taken to be 4289 mbsl based on the Snake Pit AVR), Z_{kink} is the depth at which the detachment dip changes from shallow to steep (1.5 km, based on TAG), *d1* and *d2* are the transport distances of the rocks along the shallow section and steep parts of the detachment fault, respectively, and d_{tot} is the total transport distance along the detachment fault (11.85 km, taking into account 0.354 Ma of postdetachment spreading; see section 3.4).

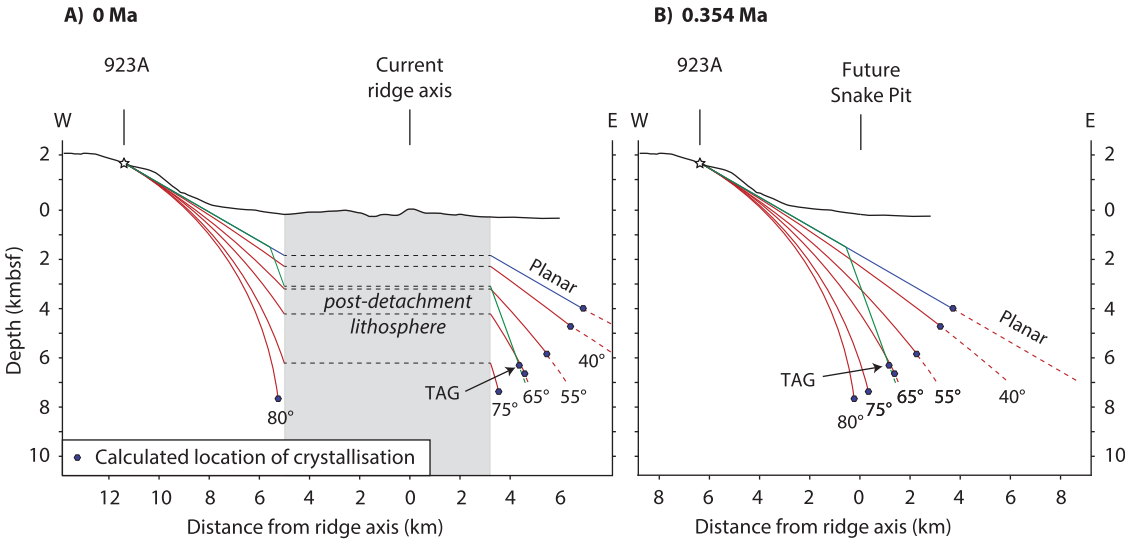

Figure 8. Reconstruction of locations of crystallization (blue symbols) for a range of detachment fault geometries. Curved geometries assume dips of 40°–80° at a depth of 7 km below seafloor and constant curvature; the TAG geometry assumes a dip of 30° of the exposed section of the detachment and a 70° dip below 1.5 km below seafloor. (a) Projection at 0 Ma of the detachment faults beneath the surface. (b) Same projection at 0.354 Ma, immediately prior to Snake Pit AVR-related magmatism cutting off the detachment. Note that for all but the steepest faults (>80° at 7 km) the detachments crossed the location of the ridge axis.

increases in sediment thickness away from the ridge axis at flow fronts of younger lava flows on older, more sedimented flows [*Gente et al*., 1991]. Finally, the morphology of the axial valley floor contrasts with that of the inferred rafted fault block along its western margin. Hence, the available data support our inference that the basalts of the axial valley floor postdate the detachment.

4.3. Spreading Rate

We consider the detailed magnetic analysis of the northern MARK segment for the last 10 Ma [*Williams*, 2007] to provide a robust long-term spreading rate for the American plate. No uncertainty is quoted for this 14.4 mm/yr rate. However, the variation in spreading rate in three different profiles provided along the study area is 0.2 mm/yr [*Williams*, 2007], and there is a 0.3 mm/yr difference between the *Williams* [2007] and *Schulz et al*. [1988] rates for the American plate. On this basis, we examine the effect of assigning an uncertainty of $\pm$0.3 mm/yr to the spreading rate (and hence slip rate) used. This propagates to an uncertainties of $\sim\pm$0.008 Ma on the duration of postdetachment spreading and $\pm$0.3 km on the crystallization depth.

The long-term American plate spreading rate of 14.4 mm/yr integrates periods of detachment faulting and periods of predominantly magmatic spreading, with the former being characterized by increased asymmetry relative to the latter [*Williams*, 2007]. By using the long-term average, we have assumed that the asymmetry during the past 1.177 Ma is the same as that during the past 10 Ma. This is not unreasonable, since the recent history studied here comprises a cycle of detachment and postdetachment spreading, like that of the long-term history. In addition, the spreading rate reconstruction shows no systematic change during the past 10 Ma [*Williams*, 2007]. What is less well constrained is the magnitude of the asymmetry during detachment-dominated versus magmatically dominated spreading. By using the 14.4 km/yr rate for both detachment and postdetachment spreading, we ignore the observation that asymmetry increases during detachment faulting [*Williams*, 2007; *Baines et al*., 2008]. We have therefore also calculated crystallization depths assuming different combinations of asymmetry (e.g., symmetric spreading postdetachment and 68% asymmetry during detachment faulting) while keeping the overall asymmetry at the observed 61.5%. We found no change in crystallization depth; the slower accretion rate of the 5.1 km of postdetachment crust leads to a shorter period of detachment faulting, canceling out the increased rate of transport along the detachment. Hence, our assumptions regarding the spreading rate asymmetry distribution do not introduce added uncertainties to our depth calculation.

4.4. U-Pb Geochronology

The effect of the uncertainties associated with the U-Pb zircon geochronology can be readily propagated to uncertainties in the calculated crystallization depths. The uncertainties in the U-Pb dates include analytical

uncertainties, uncertainties in the tracer calibration, uncertainties in the ^{238}U decay constant, and uncertainties in the data interpretation. We assumed that the weighted mean ($1.164 \pm 0.011/0.014$ Ma) of the younger zircon population of all three dated samples represents the crystallization date for the section. The 0.014 Ma external uncertainty on the weighted mean translate to an uncertainty of ± 0.2 km on the transport path the rocks have experienced along the detachment and ± 0.2 km on the crystallization depth (for a convex-upward geometry with initial dip of 65°). If we instead take the weighted means of 923A-13R-3, 65–78 cm and 923A-15R-3, 84–90 cm as the best estimates of the crystallization ages of these magmas, they would indicate crystallization depths of 6.8 and 6.4 km, respectively. This represents no change in depth for 923A-13R-3, 65–78 cm, and a $+0.4$ km shift for 923A-15R-3, 84–90 cm. Hence, the total combined uncertainty associated with the U-Pb dates is $+0.6/-0.2$ km.

4.5. Total Uncertainty

Adding up the uncertainties on detachment fault geometry (± 0.8 km), spreading rate (± 0.3 km), and U-Pb zircon dates ($+0.6/-0.2$ km), we derive a total uncertainty of $+1.7/-1.3$ km. Scenarios where the detachment has a shallow initial dip (40°), leading to shallow (4.6 km), off-axis crystallization, or where the axial valley floor is composed entirely of hanging wall blocks, leading to deep crystallization (9.8 km), are considered unlikely based on the available constraints. We therefore consider the best estimate of crystallization depth to be 6.4 $+1.7/-1.3$ km.

5. Discussion

The approach we used for calculating the crystallization depths of plutonic rocks beneath an oceanic detachment fault has been modified from *Grimes et al*. [2011] and *Schoolmeesters et al*. [2012]. All three studies combined U-Pb zircon dating with models for detachment fault geometry and plate spreading rate. However, *Grimes et al*. [2011] and *Schoolmeesters et al*. [2012] used zircon (U-Th)/He dating to determine when the gabbroic sections cooled below the 200°C isotherm. They then used the age difference between zircon U-Pb and (U-Th)/He dates and an assumed depth of the 200°C isotherm to calculate the depth of the 850°C isotherm. The depth of the 850°C isotherm, then, was taken to represent the upper limit of significant gabbro emplacement and final crystallization. In contrast, we derive crystallization depths directly from the zircon dates and tectonic constraints, without requiring (U-Th)/He data and assumptions regarding the thermal structure. Furthermore, we have used high-precision ID-TIMS for dating zircon, resulting in a more precise crystallization age (uncertainty of ± 0.01–0.02 Ma per sample) compared to the ion microprobe approach used by *Grimes et al*. [2011] (± 0.11 Ma per sample on average) and *Schoolmeesters et al*. [2012] (± 0.05 Ma per sample on average).

The crystallization depth of 6.4 $+1.7/-1.3$ km presented herein nevertheless overlaps within error with the upper limits of 7 ± 2 km derived by *Grimes et al*. [2011] and *Schoolmeesters et al*. [2012] for the oceanic core complexes in the 15°N and 30°N areas of the Mid-Atlantic Ridge. That both methods give similar results lends confidence to the assumptions made regarding the thermal structure at OCCs [*Grimes et al*., 2011; *Schoolmeesters et al*., 2012]. Although one may presuppose that crystallization depths could vary both temporally and spatially, because of variations in the rate of melt supply and hydrothermal cooling, a generic picture is appearing to emerge from a number of different Atlantic detachment fault systems that melts are emplaced into detachment fault footwalls typically at 6–7 km below the seafloor.

5.1. Footwall Capture

MacLeod et al. [2009] demonstrate that detachment faults, which typically develop into structures that accommodate >50% of total plate separation, must necessarily lengthen with time such that their active, steep, subsurface portion migrates toward and thence across the ridge axis. At this juncture, melts emplaced beneath the axis, from below or along strike, should encounter the detachment footwall rather than the hanging wall. If correct, this "footwall capture" model has important implications for hydrothermal systems associated with the detachment, since gabbro emplacement is considered an essential driver of convection along the detachment [*McCaig et al*., 2007]. In addition, as discussed by *MacLeod et al*. [2009], melt emplacement in the footwall has important implications for the magma budgets in the periods in which detachment faults form and are active. Although models suggest that detachment faulting is promoted by melt supply of 30–50% of plate separation to the hanging wall of the detachment [*Buck et al*., 2005; *Tucholke et al*., 2008],

this does not limit the total melt supply to that amount: additional melt may be emplaced into the footwall. This was confirmed in numerical models, which showed that the amount of gabbro emplacement has no effect on the formation or stability of detachment faults as long as melt emplacement by diking into the hanging wall in the brittle part of the lithosphere falls in the 30–50% window [*Olive et al*., 2010].

The tectonic reconstructions made in this paper, in addition to crystallization depths, also provide constraint upon the locus of crystallization relative to the ridge axis. This is illustrated in Figure 8, where we strip away the postdetachment lithosphere, allowing an examination of the geometry of the detachment faults relative to the ridge axis immediately prior to it being cutoff. With our preferred detachment geometry (continuous curvature projecting to a 65 ± 10° dip at 7 km depth), the detachment crossed the location of ridge axis (as determined by the future location of the Snake Pit AVR) by 1.4 +0.8/−1.0 km, rooting beneath the opposite, eastern flank. In the low dip geometrical end-member of a detachment fault with 40° initial dip, this increases to 3.2 km. Only detachment faults with the steepest initial dip allowed by the available constraints (80°) root directly beneath the ridge axis. Hence, it appears likely that the detachment fault indeed rooted on the opposite side of the ridge axis, as has been inferred for the 13°N core complexes [*MacLeod et al*., 2009], and that the magma chamber in which the Hole 923A gabbro crystallized was emplaced into the footwall of the detachment. The data presented in this paper, along with the presence of substantial gabbro bodies at oceanic core complexes (e.g., Atlantis Bank [*Dick et al*., 2000], Atlantis Massif [*Ildefonse et al*., 2007; *Blackman et al*., 2011] and 15°45′N [*MacLeod et al*., 2002; *Escartín et al*., 2003]), therefore support the hypothesis [*MacLeod et al*., 2009] that footwall melt capture is likely to be a significant process in "Chapman-type" detachment-dominated oceanic lithosphere [*Escartin and Canales*, 2011].

5.2. Melt Emplacement Depth and Lithospheric Architecture

The dates presented in this paper mark the time of zircon crystallization in the samples. The fact that the dates for the gabbro and crosscutting diorite veins overlap, and that there is at most a 0.030 ± 0.019 Ma age difference between two of the different units that have been recognized in Hole 923A [*Cannat et al*., 1995], suggests that we have captured a representative date for zircon crystallization in the section. The average crystallization temperature of oceanic zircon, determined by Ti-in-zircon thermometry, is 790°C (data in *Grimes et al*. [2009]). Hence, they form during the latest stage of crystallization in oceanic magma chambers, postdating the emplacement of primitive melt. This is consistent with the evolved nature of the dated samples (oxide and orthopyroxene-bearing gabbro and diorite). Assuming a primitive melt temperature of 1237°C (the liquidus temperature of a basalt with 10% MgO at 2 kbar, calculated using *Sugawara* [2000, equation (3)]), these melts would have cooled by 447°C between emplacement and zircon crystallization. Ca-in-olivine geospeedometry data provide an average cooling rate of 4278°C/Ma for the plutonic rocks from Hole 923A over the temperature interval 1000–600°C (data in *Coogan et al*. [2007]). Utilizing these constraints it follows that melt emplacement predated zircon crystallization by 0.104 Ma. Since the cooling rate at T > 1000°C was likely higher than the 4278°C/Ma used in this calculation, the time span of 0.104 Ma represents an upper limit. If magma chambers are emplaced in the footwall of a detachment fault, as was likely the case for the Hole 923A gabbros (Figure 8), they would be uplifted with the footwall. In this scenario, the <0.104 Ma time span between melt emplacement and zircon crystallization implies that melt emplacement depths are up to 1.5 km deeper than the crystallization depth recorded by zircon. From this we deduce that hence, our data constrain the emplacement depth of the parental melts to the Hole 923A gabbros to be 6.4–8 km.

Noting the melt emplacement depth of 6.4–8 km, and the gabbros' close spatial association with mantle peridotites, now exposed on the seafloor immediately south of Hole 923A [*Mével et al*., 1991; *Karson and Lawrence*, 1997b] (see Figure 1), it is evident that the plutonic rocks crystallized in the lithospheric mantle beneath the ridge axis during detachment-dominated spreading in the MARK area. This would have led to a lithospheric architecture of discrete gabbroic bodies in peridotite [*Cannat*, 1996], as has also been observed at the Kane megamullion, the ~2 Ma core complex west of the RTI massif [*Dick et al*., 2008; *Canales*, 2010], as well as core complexes elsewhere [*MacLeod et al*., 2002; *Escartín et al*., 2003; *Kelemen et al*., 2004; *Canales et al*., 2008]. The melt emplacement in the lithospheric mantle at ~1.2 Ma reconstructed for the MARK RTI massif contrasts with the depths of magma bodies beneath the current ridge axis; seismic data suggest the presence of partial melt between 2 and 5 km beneath the magmatically active Snake Pit AVR at 23°20′N [*Canales et al*., 2000]. Similar observations have been made at other magmatically robust Mid-Atlantic Ridge segments; at the Lucky Strike segment (37°N) a magma chamber was imaged at ~3 km

depth using seismic reflection data [*Singh et al*., 2006], and at OH-1 (35°N) seismic tomography suggests a partial melt reservoir to be present at 5 km depth [*Dunn et al*., 2005]. Combined, these observations lead to two important inferences. First, it reinforces the assertion that magmatically dominated and detachment-dominated spreading represent two fundamentally different modes of crustal accretion, leading to different lithospheric architecture [*Escartin et al*., 2008; *Escartin and Canales*, 2011]. Second, the northern spreading cell in the MARK area preserves the switch from detachment-dominated spreading with deep (6.4 km) crystallization to magmatically dominated spreading with shallow (∼2 km) crystallization [*Canales et al*., 2000]. This temporal switch in mode of accretion at the Kane ridge-transform intersection is superimposed on ridge-parallel changes in accretion documented along the first ∼80 km south of the Kane transform [*Karson et al*., 1987], indicating that temporal as well as spatial changes in melt supply and tectonics control crustal accretion.

6. Conclusions

High-precision zircon dates for plutonic rocks recovered from beneath an oceanic detachment fault exposed on the western flank of the Mid-Atlantic Ridge (MARK area, 23°N), in conjunction with a tectonic reconstruction of the MARK ridge-transform intersection, have led to the following conclusions:

1. The plutonic crust exposed at by the RTI massif detachment south of the Kane Fracture Zone yields single grain $^{206}Pb/^{238}U$ dates of 1.138 ± 0.062 to 1.213 ± 0.021 Ma;
2. The best estimate of the crystallization depth of the gabbroic rocks, calculated assuming a detachment geometry characterized by constant curvature to 65 ± 10° at 7 km depth, is 6.4 km;
3. Based on uncertainties in zircon dates, detachment geometry, and spreading rate, the crystallization depth of 6.4 km is subject to an uncertainty of +1.7/−1.3 km;
4. The melt parental to the sampled gabbroic rocks was emplaced up to 1.5 km below the final crystallization gabbro depth (i.e., as much as 8 km depth);
5. With the exception of the steepest possible detachment geometries (≥80° dip at 7 km depth), the structural reconstructions indicate that the detachment fault rooted on the eastern side of the ridge axis by 1.4 +0.8/−1.0 km when it was active, thus crossing the ridge axis. This supports the concept that footwall capture—melt emplacement into the footwall of active detachment faults—is an important part of the evolution of oceanic detachment systems.
6. The 6.4–8 km melt emplacement depth during detachment-dominated spreading at ∼1.2 Ma contrasts with the presence of partial melt at ∼2–5 km beneath the currently active, magmatically robust ridge axis; hence, the northern MARK segment preserves a temporal switch from detachment mode of accretion characterized by deep melt emplacement to magmatic mode of crustal accretion with shallow magma reservoirs.

Acknowledgments
This research used samples and/or data provided by the Ocean Drilling Program (ODP). ODP was sponsored by the U.S. National Science Foundation (NSF) and participating countries under management of Joint Oceanographic Institutions (JOI), Inc. This work was supported by NERC grant NE/H020004/1 to C.J.L. and a WHOI Deep Ocean Exploration Institute grant to N.S. We thank three anonymous reviewers for their in-depth comments.

References

Allerton, S., J. Escartín, and R. Searle (2000), Extremely asymmetric magmatic accretion of oceanic crust at the ends of slow-spreading ridge segments, *Geology*, *28*, 179–182, doi:10.1130/0091-7613(2000)28<179:EAMAOO>2.0.CO;2.

Auzende, J.-M., M. Cannat, P. Gente, J.-P. Henriet, T. Juteau, J. Karson, Y. Lagabrielle, C. Mével, and M. Tivey (1994), Observation of sections of oceanic crust and mantle cropping out on the southern wall of Kane FZ (N. Atlantic), *Terra Nova*, *6*, 143–148.

Baines, A. G., M. J. Cheadle, B. E. John, and J. J. Schwartz (2008), The rate of oceanic detachment faulting at Atlantis Bank, SW Indian Ridge, *Earth Planet. Sci. Lett.*, *273*(1-2), 105–114.

Ballu, V., J. Dubois, C. Deplus, M. Diament, and S. Bonvalot (1998), Crustal structure of the Mid-Atlantic Ridge south of the Kane Fracture Zone from seafloor and sea surface gravity data, *J. Geophys. Res.*, *103*(B2), 2615–2631.

Behn, M. D., and G. Ito (2008), Magmatic and tectonic extension at mid-ocean ridges: 1. Controls on fault characteristics, *Geochem. Geophys. Geosyst.*, *9*, Q08O10, doi:10.1029/2008GC001965.

Blackman, D. K., et al. (2011), Drilling constraints on lithospheric accretion and evolution at Atlantis Massif, Mid-Atlantic Ridge 30°N, *J. Geophys. Res.*, *116*, B07103, doi:10.1029/2010JB007931.

Bowring, J. F., N. M. McLean, and S. A. Bowring (2011), Engineering cyber infrastructure for U-Pb geochronology: Tripoli and U-Pb_Redux, *Geochem. Geophys. Geosyst.*, *12*, Q0AA19, doi:10.1029/2010GC003479.

Brown, J. R., and J. A. Karson (1988), Variations in axial processes on the Mid-Atlantic Ridge: The median valley of the MARK area, *Mar. Geophys. Res.*, *10*(1–2), 109–138.

Buck, W. R., L. L. Lavier, and A. N. B. Poliakov (2005), Modes of faulting at mid-ocean ridges, *Nature*, *434*(7034), 719–723.

Canales, J. P. (2010), Small-scale structure of the Kane oceanic core complex, Mid-Atlantic Ridge 23°30′N, from waveform tomography of multichannel seismic data, *Geophys. Res. Lett.*, *37*, L21305, doi:10.1029/2010GL044412.

Canales, J. P., J. A. Collins, J. Escartin, and R. S. Detrick (2000), Seismic structure across the rift valley of the Mid-Atlantic Ridge at 23 degrees 20′ (MARK area): Implications for crustal accretion processes at slow spreading ridges, *J. Geophys. Res.*, *105*(12), 28,411–28,425.

Canales, J. P., B. E. Tucholke, M. Xu, J. A. Collins, and D. L. DuBois (2008), Seismic evidence for large-scale compositional heterogeneity of oceanic core complexes, *Geochem. Geophys. Geosyst.*, *9*, Q08002, doi:10.1029/2008GC002009.
Cann, J. R., D. K. Blackman, D. K. Smith, E. McAllister, B. Janssen, S. Mello, E. Avgerinos, A. R. Pascoe, and J. Escartin (1997), Corrugated slip surfaces formed at ridge-transform intersections on the Mid-Atlantic Ridge, *Nature*, *385*, 329–332.
Cann, J. R., D. K. Smith, J. Escartin, and H. Schouten (2015), Tectonic evolution of 200 km of Mid-Atlantic Ridge over 10 million years—Interplay of volcanism and faulting, *Geochem. Geophys. Geosyst.*, *16*, 2303–2321, doi:10.1002/2015GC005797.
Cannat, M. (1996), How thick is the magmatic crust at slow spreading oceanic ridges, *J. Geophys. Res.*, *101*(B2), 2847–2857.
Cannat, M., et al. (Eds.) (1995), *Proceedings of the Ocean Drilling Program, Initial Reports*, vol. 153, 798 pp., Ocean Drill. Program, College Station, Tex.
Cannat, M., D. Sauter, V. Mendel, E. Ruellan, K. Okino, J. Escartin, V. Combier, and M. Baala (2006), Modes of seafloor generation at a melt-poor ultraslow-spreading ridge, *Geology*, *34*(7), 605–608, doi:10.1130/G22486.1.
Casey, J. F. (1997), Comparison of major- and trace-element geochemistry of abyssal peridotites and mafic plutonic rocks with basalts from the MARK region of the Mid-Atlantic Ridge, in *Proceedings of the Ocean Drilling Program, Scientific Results*, edited by J. A. Karson et al., pp. 181-241, Ocean Drill. Program, College Station, Tex.
Condon, D. J., B. Schoene, N. M. McLean, S. A. Bowring, and R. R. Parrish (2015), Metrology and traceability of U-Pb isotope dilution geochronology (EARTHTIME Tracer Calibration Part I), *Geochimica et Cosmochimica Acta*, *164*, 464–480, doi:10.1016/j.gca.2015.05.026.
Coogan, L. A., A. D. Saunders, P. D. Kempton, and M. J. Norry (2000), Evidence from oceanic gabbros for porous melt migration within a crystal mush beneath the Mid-Atlantic Ridge, *Geochem. Geophys. Geosyst.*, *1*(9), 1044, doi:10.1029/2000GC000072.
Coogan, L. A., G. R. T. Jenkin, and R. N. Wilson (2007), Contrasting cooling rates in the lower oceanic crust at fast- and slow-spreading ridges revealed by geospeedometry, *J. Petrol.*, *48*(11), 2211–2231.
deMartin, B. J., R. A. Sohn, J. Pablo Canales, and S. E. Humphris (2007), Kinematics and geometry of active detachment faulting beneath the Trans-Atlantic Geotraverse (TAG) hydrothermal field on the Mid-Atlantic Ridge, *Geology*, *35*(8), 711–714.
Detrick, R., et al. (1988), *Proceedings of the Ocean Drilling Program, Initial Reports*, vol. 106/109, Ocean Drill. Program, College Station, Tex.
Detrick, R. S., and G. M. Purdy (1980), The crustal structure of the Kane Fracture Zone from seismic refraction studies, *J. Geophys. Res.*, *85*(B7), 3759–3777.
Detrick, R. S., J. C. Mutter, P. Buhl, and I. I. Kim (1990), No evidence from multichannel reflection data for a crustal magma chamber in the MARK area on the Mid-Atlantic Ridge, *Nature*, *347*, 61–64.
Dick, H. J. B., W. B. Bryan, and G. Thompson (1981), Low-angle faulting and steady-state emplacement of plutonic rocks at ridge-transform intersections, *Eos Trans. AGU*, *62*, 406.
Dick, H. J. B., et al. (2000), A long in-situ section of the lower ocean crust: Results of ODP Leg 176 Drilling at the Southwest Indian Ridge, *Earth Planet. Sci. Lett.*, *179*, 31–51.
Dick, H. J. B., M. A. Tivey, and B. E. Tucholke (2008), Plutonic foundation of a slow-spread ridge segment: The oceanic core complex at Kane Megamullion, 23°30′N, 45°20′W, *Geochem. Geophys. Geosyst.*, *9*, Q05014, doi:10.1029/2007GC001645.
Dunn, R. A., V. Lekic, R. S. Detrick, and D. R. Toomey (2005), Three-dimensional seismic structure of the Mid-Atlantic Ridge (35°N): Evidence for focused melt supply and lower crustal dike injection, *J. Geophys. Res.*, *110*, B09101, doi:10.1029/2004JB003473.
Escartin, J., and J. P. Canales (2011), Detachments in oceanic lithosphere: Deformation, magmatism, fluid flow and ecosystems, *Eos Trans. AGU*, *92*(4), 31, doi:10.1029/2011EO040003.
Escartín, J., C. Mével, C. J. MacLeod, and A. M. McCaig (2003), Constraints on deformation conditions and the origin of oceanic detachments: The Mid-Atlantic Ridge core complex at 15°45′N, *Geochem. Geophys. Geosyst.*, *4*(8), 1067, doi:10.1029/2002GC000472.
Escartin, J., D. K. Smith, J. Cann, H. Schouten, C. H. Langmuir, and S. Escrig (2008), Central role of detachment faults in accretion of slow-spreading oceanic lithosphere, *Nature*, *455*(7214), 790–794.
Fletcher, J., G. Ceuleneer, and M. Cannat (1997), Microfabrics and patterns of dynamic recrystallization in gabbroic rocks from the MARK area, Mid-Atlantic Ridge, in *Proceedings of Ocean Drilling Program, Sci. Results*, vol. 153, edited by J. A. Karson et al., pp. 143–153, Ocean Drill. Program, College Station, Tex.
Gente, P., C. Mevel, J. M. Auzende, J. A. Karson, and Y. Fouquet (1991), An example of a recent accretion on the Mid-Atlantic Ridge: The Snakepit neovolcanic ridge (MARK area, 23°22′N), *Tectonophysics*, *190*, 1–29.
Gente, P., R. A. Pockalny, C. Durand, C. Deplus, M. Maia, G. Ceuleneer, C. Mével, M. Cannat, and C. Laverne (1995), Characteristics and evolution of the segmentation of the Mid-Atlantic Ridge between 20°N and 24°N during the last 10 million years, *Earth Planet. Sci. Lett.*, *129*(1–4), 55–71.
Grimes, C. B., B. E. John, M. Cheadle, and J. L. Wooden (2008), Protracted construction of gabbroic crust at a slow-spreading ridge: Constraints from 206Pb/238U zircon ages from Atlantis Massif and IODP Hole U1309D (30°N, MAR), *Geochem. Geophys. Geosyst.*, *9*, Q08012, doi:10.1029/2008GC002063.
Grimes, C. B., B. John, M. Cheadle, F. Mazdab, J. Wooden, S. Swapp, and J. Schwartz (2009), On the occurrence, trace element geochemistry, and crystallization history of zircon from in situ ocean lithosphere, *Contrib. Mineral. Petrol.*, *158*(6), 757–783.
Grimes, C. B., M. J. Cheadle, B. E. John, P. W. Reiners, and J. L. Wooden (2011), Cooling rates and the depth of detachment faulting at oceanic core complexes: Evidence from zircon Pb/U and (U-Th)/He ages, *Geochem. Geophys. Geosyst.*, *12*, Q0AG01, doi:10.1029/2010GC003391.
Harper, G. D. (1985), Tectonics of slow spreading mid-ocean ridges and consequences of a variable depth to the brittle/ductile transition, *Tectonics*, *4*(4), 395–409.
Hiess, J., D. J. Condon, N. M. McLean, and S. R. Noble (2012), 238U/235U systematics in terrestrial uranium-bearing minerals, *Science*, *335*(6076), 1610–1614, doi:10.1126/science.1215507.
Ildefonse, B., D. K. Blackman, B. E. John, Y. Ohara, D. J. Miller, C. J. MacLeod, and Integrated Ocean Drilling Program Expeditions 304/305 Science Party (2007), Oceanic core complexes and crustal accretion at slow-spreading ridges, *Geology*, *35*(7), 623–626.
Jaffey, A. H., K. F. Flynn, L. E. Glendenin, W. C. Bentley, and A. M. Essling (1971), Precision Measurement of Half-Lives and Specific Activities of ^{235}U and ^{238}U, *Physical Review C*, *4*(5), 1889–1906.
Karson, J. A., and J. R. Brown (1988), Geologic setting of the Snake Pit hydrothermal site: An active vent field on the Mid-Atlantic Ridge, *Mar Geophys Res*, *10*(1–2), 91–107.
Karson, J. A., and H. J. B. Dick (1983), Tectonics of ridge-transform intersections at the Kane Fracture Zone, *Mar Geophys Res*, *6*, 51–98.
Karson, J. A., and R. M. Lawrence (1997a), Tectonic window into gabbroic rocks of the middle oceanic crust in the MARK area near Sites 921–924, in *Proc. ODP, Sci. Results, 153*, edited by J. A. Karson, M. Cannat, D. J. Miller and D. Elthon, pp. 61–76, Ocean Drilling Program, College Station, Tex.

Karson, J. A., and R. M. Lawrence (1997b), Tectonic setting of serpentinite exposures on the western median valley wall of the MARK area in the vicinity of Site 920, in *Proc. ODP, Sci. Results, 153*, edited by J. A. Karson, M. Cannat, D. J. Miller and D. Elthon, pp. 5–22, Ocean Drilling Program, College Station, Tex.

Karson, J. A., et al. (1987), Along-axis variations in seafloor spreading in the MARK area, *Nature*, *328*, 681–685.

Kelemen, P. B., E. Kikawa, D. J. Miller, and et al. (2004), *Proceedings of the Ocean Drilling Program, Initial Reports, 209*, Ocean Drilling Program, Texas A&M University, College Station, TX 77845-9547.

Kong, L. S. L., R. S. Detrick, P. J. Fox, L. A. Mayer, and W. B. F. Ryan (1988), The morphology and tectonics of the Mark Area from Sea Beam and Sea MARC I observations (Mid-Atlantic Ridge 23°N), *Mar Geophys Res*, *10*, 59–90.

Kong, L. S. L., S. C. Solomon, and G. M. Purdy (1992), Microearthquake characteristics of a mid-ocean ridge along-axis high, *J. Geophys. Res.*, *97*(B2), 1659–1685.

Lavier, L. L., W. Roger Buck, and A. N. B. Poliakov (1999), Self-consistent rolling-hinge model for the evolution of large-offset low-angle normal faults, *Geology*, *27*(12), 1127–1130.

Lissenberg, C. J., M. Rioux, N. Shimizu, S. A. Bowring, and C. Mevel (2009), Zircon Dating of Oceanic Crustal Accretion, *Science*, *323*(5917), 1048–1050.

MacLeod, C. J., et al. (2002), Direct geological evidence for oceanic detachment faulting: The Mid-Atlantic Ridge, 15°45′ N, *Geology*, *30*(10), 879–882.

MacLeod, C. J., R. C. Searle, B. J. Murton, J. F. Casey, C. Mallows, S. C. Unsworth, K. L. Achenbach, and M. Harris (2009), Life cycle of oceanic core complexes, *Earth Planet. Sci. Lett.*, *287*(3–4), 333–344.

MacLeod, C. J., J. Carlut, J. Escartín, H. Horen, and A. Morris (2011), Quantitative constraint on footwall rotations at the 15°45′N oceanic core complex, Mid-Atlantic Ridge: Implications for oceanic detachment fault processes, *Geochem. Geophys. Geosyst.*, *12*, Q0AG03, doi:10.1029/2011GC003503.

Mattinson, J. M. (2005), Zircon U-Pb chemical abrasion (''CA-TIMS'') method: Combined annealing and multi-step partial dissolution analysis for improved precision and accuracy of zircon ages, *Chem. Geol.*, *220*(1–2), 47–66.

McCaig, A. M., R. A. Cliff, J. Escartin, A. E. Fallick, and C. J. MacLeod (2007), Oceanic detachment faults focus very large volumes of black smoker fluids, *Geology*, *35*(10), 935–938.

McLean, N. M., J. F. Bowring, and S. A. Bowring (2011), An algorithm for U-Pb isotope dilution data reduction and uncertainty propagation, *Geochem. Geophys. Geosyst.*, *12*, Q0AA18, doi:10.1029/2010GC003478.

McLean, N. M., D. J. Condon, B. Schoene, and S. A. Bowring (2015), Evaluating uncertainties in the calibration of isotopic reference materials and multi-element isotopic tracers (EARTHTIME Tracer Calibration Part II), *Geochimica et Cosmochimica Acta*, *164*, 481–501, doi:10.1016/j.gca.2015.02.040.

Mével, C., M. Cannat, P. Gente, E. Marion, J. M. Auzende, and J. A. Karson (1991), Emplacement of deep crustal and mantle rocks on the west wall of the MARK area (Mid-Atlantic Ridge, 23°N), *Tectonophysics*, *190*, 31–53.

Morris, A., J. S. Gee, N. Pressling, B. E. John, C. J. MacLeod, C. B. Grimes, and R. C. Searle (2009), Footwall rotation in an oceanic core complex quantified using reoriented Integrated Ocean Drilling Program core samples, *Earth Planet. Sci. Lett.*, *287*(1–2), 217–228.

Okino, K., K. Matsuda, D. M. Christie, Y. Nogi, and K.-I. Koizumi (2004), Development of oceanic detachment and asymmetric spreading at the Australian-Antarctic Discordance, *Geochem. Geophys. Geosyst.*, *5*, Q12012, doi:10.1029/2004GC000793.

Olive, J.-A., M. D. Behn, and B. E. Tucholke (2010), The structure of oceanic core complexes controlled by the depth distribution of magma emplacement, *Nat. Geosci.*, *3*(7), 491–495.

Pockalny, R. A., R. S. Detrick, and P. J. Fox (1988), Morphology and tectonics of the Kane Transform from sea beam bathymetry data, *J. Geophys. Res.*, *93*(B4), 3179–3193.

Purdy, G. M., and R. S. Detrick (1986), Crustal structure of the Mid-Atlantic Ridge at 23°N from seismic refraction studies, *J. Geophys. Res.*, *91*(B3), 3739–3762.

Ranero, C. R., and T. J. Reston (1999), Detachment faulting at ocean core complexes, *Geology*, *27*(11), 983–986.

Rioux, M., C. J. Lissenberg, N. McLean, S. A. Bowring, C. J. MacLeod, E. Hellebrand, and N. Shimizu (2012), Protracted timescales of lower crustal growth at the fast-spreading East Pacific Rise, *Nat. Geosci.*, *5*(4), 275–278.

Rioux, M., S. A. Bowring, M. J. Cheadle, and B. E. John (2015a), Evidence for initial excess ^{231}Pa in mid-ocean ridge zircons, *Chem. Geol.*, *397*, 143–156.

Rioux, M., N. Jöns, S. Bowring, C. J. Lissenberg, W. Bach, A. Kylander-Clark, B. Hacker, and F. Dudás (2015b), U-Pb dating of interspersed gabbroic magmatism and hydrothermal metamorphism during lower crustal accretion, Vema lithospheric section, Mid-Atlantic Ridge, *J. Geophys. Res. Solid Earth*, *120*, 2093–2118, doi:10.1002/2014JB011668.

Ross, K., and D. Elthon (1997), Cumulus and postcumulus crystallization in the oceanic crust: Major- and trace-element geochemistry of Leg 153 gabbros, in *Proceedings of the Ocean Drilling Program, Scientific Results*, vol. 153, edited by J. A. Karson, et al., pp. 333–350, Ocean Drill. Program, College Station, Tex.

Ryan, W. B. F., et al. (2009), Global Multi-Resolution Topography synthesis, *Geochem. Geophys. Geosyst.*, *10*, Q03014, doi:10.1029/2008GC002332.

Sauter, D., et al. (2013), Continuous exhumation of mantle-derived rocks at the Southwest Indian Ridge for 11 million years, *Nat. Geosci.*, *6*(4), 314–320.

Schoolmeesters, N., M. J. Cheadle, B. E. John, P. W. Reiners, J. Gee, and C. B. Grimes (2012), The cooling history and the depth of detachment faulting at the Atlantis Massif oceanic core complex, *Geochem. Geophys. Geosyst.*, *13*, Q0AG12, doi:10.1029/2012GC004314.

Schulz, N. J., R. S. Detrick, and S. P. Miller (1988), Two- and three-dimensional inversions of magnetic anomalies in the MARK area (Mid-Atlantic Ridge 23°N), *Mar. Geophys. Res.*, *10*, 41–57.

Schwartz, J. J., B. E. John, M. J. Cheadle, E. A. Miranda, C. B. Grimes, J. L. Wooden, and H. J. B. Dick (2005), Dating the Growth of Oceanic Crust at a Slow-Spreading Ridge, *Science*, *310*(5748), 654–657.

Searle, R. C., M. Cannat, K. Fujioka, C. Mével, H. Fujimoto, A. Bralee, and L. Parson (2003), FUJI Dome: A large detachment fault near 64°E on the very slow-spreading southwest Indian Ridge, *Geochem. Geophys. Geosyst.*, *4*(8), 9105, doi:10.1029/2003GC000519.

Severinghaus, J. P., and K. C. Macdonald (1988), High inside corners at ridge-transform intersections, *Mar. Geophys. Res.*, *9*, 353–367.

Singh, S. C., W. C. Crawford, H. Carton, T. Seher, V. Combier, M. Cannat, J. Pablo Canales, D. Dusunur, J. Escartin, and J. Miguel Miranda (2006), Discovery of a magma chamber and faults beneath a Mid-Atlantic Ridge hydrothermal field, *Nature*, *442*(7106), 1029–1032.

Smith, D. K., J. R. Cann, and J. Escartin (2006), Widespread active detachment faulting and core complex formation near 13°N on the Mid-Atlantic Ridge, *Nature*, *442*(7101), 440–443.

Sturm, M. E., S. J. Goldstein, E. M. Klein, J. A. Karson, and M. T. Murrell (2000), Uranium-series age constraints on lavas from the axial valley of the Mid-Atlantic Ridge, MARK area, *Earth Planet. Sci. Lett.*, *181*, 61–70.

Sugawara, T. (2000), Empirical relationships between temperature, pressure, and MgO content in olivine and pyroxene saturated liquid, *J. Geophys. Res.*, *105*(B4), 8457–8472.

Tucholke, B. E., and J. Lin (1994), A geological model for the structure of ridge segments in slow spreading ocean crust, *J. Geophys. Res.*, *99*(B6), 11,937–11,958.

Tucholke, B. E., J. Lin, and M. C. Kleinrock (1998), Megamullions and mullion structure defining oceanic metamorphic core complexes on the Mid-Atlantic Ridge, *J. Geophys. Res.*, *103*(B5), 9857–9866.

Tucholke, B. E., M. D. Behn, W. R. Buck, and J. Lin (2008), Role of melt supply in oceanic detachment faulting and formation of megamullions, *Geology*, *36*(6), 455–458.

Williams, C. M. (2007), *Oceanic Lithosphere Magnetization: Marine Magnetic Investigations of Crustal Accretion and Tectonic Processes in Mid-Ocean Ridge Environments*, PhD thesis, 254 pp., Mass. Inst. of Technol., Woods Hole Oceanogr. Inst., Woods Hole.

Wolfe, C. J., G. M. Purdy, D. R. Toomey, and S. C. Solomon (1995), Microearthquake characteristics and crustal velocity structure at 29°N on the Mid-Atlantic Ridge: The architecture of a slow spreading segment, *J. Geophys. Res.*, *100*(B12), 24,449–24,472.